Systems/Circuits

Coupled Dynamics of Stimulus-Evoked Gustatory Cortical and Basolateral Amygdalar Activity

Abuzar Mahmood,[1] **Jessica Steindler,**[2] **Hannah Germaine,**[1] **Paul Miller,**[1,3,4] **and Donald B. Katz**[1,2,4]
[1]Graduate Program in Neuroscience, Brandeis University, Waltham, Massachusetts 02453, [2]Departments of Psychology and, [3]Biology, Brandeis University, Waltham, Massachusetts 02453, and [4]Volen Center for Complex Systems, Brandeis University, Waltham, Massachusetts 02453

Gustatory cortical (GC) single-neuron taste responses reflect taste quality and palatability in successive epochs. Ensemble analyses reveal epoch-to-epoch firing-rate changes in these responses to be sudden, coherent transitions. Such nonlinear dynamics suggest that GC is part of a recurrent network, producing these dynamics in concert with other structures. Basolateral amygdala (BLA), which is reciprocally connected to GC and central to hedonic processing, is a strong candidate partner for GC, in that BLA taste responses evolve on the same general clock as GC and because inhibition of activity in the BLA→GC pathway degrades the sharpness of GC transitions. These facts motivate, but do not test, our overarching hypothesis that BLA and GC act as a single, comodulated network during taste processing. Here, we provide just this test of simultaneous (BLA and GC) extracellular taste responses in female rats, probing the multiregional dynamics of activity to directly test whether BLA and GC responses contain coupled dynamics. We show that BLA and GC response magnitudes covary across trials and within single responses, and that changes in BLA–GC local field potential phase coherence are epoch specific. Such classic coherence analyses, however, obscure the most salient facet of BLA–GC coupling: sudden transitions in and out of the epoch known to be involved in driving gaping behavior happen near simultaneously in the two regions, despite huge trial-to-trial variability in transition latencies. This novel form of inter-regional coupling, which we show is easily replicated in model networks, suggests collective processing in a distributed neural network.

Key words: **changepoint models; coherence; gustatory; multiregion; taste; transition**

Significance Statement

There has been little investigation into real-time communication between brain regions during taste processing, a fact reflecting the dominant belief that taste circuitry is largely feedforward. Here, we perform an in-depth analysis of real-time interactions between GC and BLA in response to passive taste deliveries, using both conventional coherence metrics and a novel methodology that explicitly considers trial-to-trial variability and fast single-trial dynamics in evoked responses. Our results demonstrate that BLA–GC coherence changes as the taste response unfolds, and that BLA and GC specifically couple for the sudden transition into (and out of) the behaviorally relevant neural response epoch, suggesting (although not proving) that: (1) recurrent interactions subserve the function of the dyad as (2) a putative attractor network.

Introduction

As a rat feeds, gustatory cortical (GC) single-neuron taste responses take the form of a sequence of distinct epochs separated by sudden ensemble transitions. The epoch that starts at 0.5–1.5 s (depending on the trial) contains firing that is staunchly palatability related; the transition into that epoch, which is so sudden that it is analytically indistinguishable from state switching (Sadacca et al., 2016; see below for distinction of the terms epoch and state), both predicts and drives taste-related oral behavior (Sadacca et al., 2012; Li et al., 2016; Mukherjee et al., 2019). Theory suggests that such dynamics are most easily generated by a distributed circuit in which strong recurrent connectivity (Maass et al., 2007; Miller and Katz, 2010, 2013; Edelman and Gally, 2013; Mante et al., 2013; Kietzmann et al., 2019) couples separate regions into a single processing unit; such recurrence is abundant within the taste circuit (Bielavska and Roldan, 1996; McDonald, 1998; Shi and Cassell, 1998).

Particularly notable in this regard is the reciprocally connected GC–basolateral amygdala (BLA) dyad. Work investigating these

Received July 20, 2022; revised Nov. 12, 2022; accepted Nov. 15, 2022.

Author contributions: A.M., P.M., and D.B.K. designed research; A.M., J.S., H.G., and P.M. performed research; A.M. and D.B.K. contributed unpublished reagents/analytic tools; A.M., H.G., P.M., and D.B.K. analyzed data; A.M. and D.B.K. wrote the paper.

This work was supported by National Institutes of Health–National Institute of Deafness and Other Communication Disorders Grant DC006666 (D.B.K.). For data analysis, we used the Extreme Science and Engineering Discovery Environment, which is supported by National Science Foundation Grant IBN180002. We thank the members of Katz Laboratory for input, in particular, Drs. Jian-You Lin and Bradly Stone for discussion and guidance.

The authors declare no competing financial interests.

Correspondence should be addressed to Donald B. Katz at dbkatz@brandeis.edu.

https://doi.org/10.1523/JNEUROSCI.1412-22.2022

brain regions separately (Katz et al., 2001; Fontanini et al., 2009; Sadacca et al., 2012) has revealed striking similarities in the trial-averaged dynamics of their taste responses. Furthermore, BLA–GC connectivity has proven important for both taste learning (Lin and Reilly, 2012; Lin et al., 2015; Lavi et al., 2018; Kayyal et al., 2019) and taste processing (Lin et al., 2021). This latter study specifically demonstrated that the suddenness of the behaviorally relevant GC ensemble transitions to the palatability epoch is degraded by inhibition of BLA→GC axons. These results provide indirect evidence for a general hypothesis that BLA and GC work together during taste processing but stop far short of testing the existence of dynamic BLA-GC coupling; in fact, there has been little work directly investigating communication between any pair of taste-relevant brain regions (but see Di Lorenzo and Monroe, 1997).

Work investigating pairs of regions involved in other processes—decision-making (Antzoulatos and Miller, 2016; Place et al., 2016; Zielinski et al., 2019), sensory-motor transformation (Arce-McShane et al., 2016), vision (Bastos et al., 2015; Zandvakili and Kohn, 2015; Saravani et al., 2019; Lundqvist et al., 2020), and motor planning (Yates et al., 2017; Ames and Churchland, 2019)—has revealed inter-regional spiking and field potential coherence but has done so using metrics for which temporal resolution, particularly at the single-trial level, is limited. Given the epochal nature of taste processing, the suddenness of GC ensemble transitions into palatability responsiveness, and the trial-specific latency of this transition, testing GC–BLA coupling requires techniques that permit evaluation of the moment-to-moment evolution of the BLA–GC relationship. The fact that the suddenness of GC ensemble transitions (Sadacca et al., 2016; Mukherjee et al., 2019) depends on an intact BLA→GC pathway (Lin et al., 2021) motivates our novel, central prediction, that this moment of transition will be coupled across BLA–GC ensembles.

Here, we present an in-depth investigation of BLA–GC taste–response coordination, beginning with canonical methods [correlations of spiking in whole trials and phase coherence of local field potentials (LFP) across trials] and progressing to the testing of our novel hypothesis. The former allows us to show trial-specific and time-varying coupling in BLA and GC taste responses—reductions in phase coherence (Stitt et al., 2017) that appear and vanish in an epoch-specific manner. But because these analyses necessarily obscure coupling in the trial-specific timing of sudden state-to-state ensemble transitions, we move on to explicit modeling of state transitions in ensemble time series data (Rabiner, 1989; Sadacca et al., 2016); these analyses allow us to confirm our prediction that BLA–GC coordination integrally involves sudden, brief coupling of the specific transitions that predict and drive palatability-related behavior. Finally, computational modeling demonstrates that these results (coordinated state transitions with variable statewise functional connectivity) are easily recapitulated within a simple multiregion network. These results overall lead us to suggest that BLA and GC form a functional unit for purposes of taste processing.

Materials and Methods

Experimental design and statistical analyses

Subjects

Adult, female Long–Evans rats ($n = 8$, 300–350 g at time of electrode implantation, Charles River Laboratories) served as subjects in our study. (We have observed no sex differences in the basic cortical dynamics of taste responses between male and female rats, and therefore use female Long–Evans rats because they are, in our hands, calmer than males.) The rats were housed in individual cages in a temperature- and humidity-controlled environment under a 12 h light/dark cycle, given access to food and water *ad libitum* before the start of experimentation, and weighed daily following surgery to ensure that they never dropped below 80% of their presurgery weight. All experimental methods were in compliance with National Institutes of Health guidelines and were approved in advance by the Brandeis University Institutional Animal Care and Use Committee.

Electrode and intraoral cannula construction

Custom microwire bundle drives were made with either 16 or 32 electrodes per recording site (design and construction details available at https://katzlab.squarespace.com/technology). Intraoral cannulae, flexible tubing with a flanged tip and washer to ensure stability, connected to a plastic top complete with a locking mechanism, were built to allow the delivery of tastants directly onto the tongue (Fontanini and Katz, 2006).

Acquisition of electrophysiological data

Electrophysiological signals from the microelectrodes were sampled at 30 kHz using 32-channel analog-to-digital converter chips (catalog #RHD2132) from Intan Technologies, digitized online at the head stage and sampled jointly, along with signals from actuators marking tastant delivery, using an Intan RHD USB interface board (catalog #C3100), which routed records to the hard drive of a PC for saving. The experimental chamber was ensconced in a Faraday cage that shielded recordings from external electromagnetic influences.

Surgery

Rats were anaesthetized with an intraperitoneal injection of ketamine/xylazine cocktail (100 mg/kg and 5.2 mg/kg, respectively) and mounted in a stereotaxic instrument (David Kopf Instruments) with blunt (atraumatic) ear bars. A midline incision exposed the skull, and trephine holes (~2 mm diameter) were drilled above BLA and GC. For six (of eight) rats, microwire bundles were implanted at the dorsal surface of GC (coordinates, AP +1.4 mm, ML −5.0 mm, DV −4.4 mm from dura) and BLA (coordinates, AP −3.0 mm, ML −5.0 mm, DV −6.8 mm from dura). For the remaining two rats, bundles were instead implanted bilaterally above BLA. Once in place, electrode bundles were cemented to the skull. Once electrode bundles were secured, an intraoral cannula (IOC) was threaded through the masseter muscle (inside the zygomatic arch) to the space between the lip and gums, and the top of the cannula was cemented to the rest of the assembly with dental acrylic (Fontanini and Katz, 2006). The body temperature of the rat was monitored and maintained at ~37°C by a heating pad throughout the duration of the surgery.

Habituation and passive taste administration

Following recovery from surgery, we habituated rats to the experimental chamber for 2 d, to the IOC/electrode harness for the next 2 d, and to passive water deliveries for the following 2 d before beginning data collection. Starting with the second habituation day, we also placed rats on a mild water restriction schedule of 20 ml of water (not including the ~4 ml delivered during habituation sessions) per day. This water restriction schedule was maintained until the end of the experiment. For the two final habituation sessions, we attached the rats to the taste delivery apparatus and infused 120 pulses of distilled water (~30 µl per pulse; 20 s interpulse interval) into the oral cavity of the animal through the IOC and drove electrode bundles deeper (by 250 µm) into target structures. By the end of this procedure, the tips of the electrodes lay within GC and BLA. We then recorded taste responses during 3–4 d of taste delivery sessions; between each session the microwire bundle was driven down ~60 µm. During these sessions, sucrose (0.3 M), sodium chloride (0.1 M), citric acid (0.1 M), and quinine (1 mM), dissolved in ultrapure water (~30 µl per pulse; 20 s interpulse interval, 30 trials/tastant) were delivered to passive rats (i.e., no behavior was required to elicit delivery). These concentrations were chosen to represent a range of hedonic values and because they are known to evoke robust responses in both GC and BLA (Fontanini et al., 2009; Sadacca et al., 2012).

Histology

In preparation for histology, rats were deeply anesthetized with an overdose of the ketamine/xylazine mixture. We perfused the rats through the

heart with 0.9% saline followed by 10% formalin and harvested the brain. The brain tissue was incubated in a fixing mixture of 30% sucrose and 10% formalin for 7 d before being sectioned into 50 µm coronal slices on a sliding microtome (Leica SM2010R, Leica Microsystems). Sections containing the electrode implant sites around GC and BLA were imaged at 2×.

Data and statistical analyses

The analysis of data and statistical tests were performed using custom-written software in Python and MATLAB R2018a (MathWorks), as described below.

Local field potential processing and analysis

Filtering/power and phase extractions

LFPs were extracted from broadband digitized signals using a second-order bandpass Butterworth filter (1–300 Hz), to de-emphasize spiking and emphasize frequencies typically of interest in such data. To avoid contamination from noise/artifacts on noisy/broken channels, only channels containing isolable single neurons (see below) were used for analyses. Estimates of instantaneous power and phase in delta (1–4 Hz), theta (4–7 Hz), mu (8–12 Hz), beta (12–30 Hz), and gamma (30–100 Hz) bands were extracting using the Short-time Fourier transform implementation in Scipy software (Virtanen et al., 2020) with a 500 ms window and 99% window overlap.

LFP phase coherence

Phase coherence analysis was performed, as per Kramer and Eden (2020), to provide a basic, dynamic, trial-averaged evaluation of BLA and GC coupling as visible in LFPs. We selected for this analysis the electrodes from which activity was most similar to the mean activity for the region (smallest mean-squared error relative to the mean phase across all channels for each region; this selection of channels was constant for all trials in a single analyzed session, and the same set of channels was used for all frequencies) to ensure reliable representation of each. The difference in phase between the (GC and BLA) pair of electrodes for each time point was calculated across all trials, and the mean of those phase-difference vectors was calculated for each time point, the magnitude of which represents the coherence strength. Coherence values were averaged across small canonically defined frequency bands, theta (4–7 Hz) and mu (8–12 Hz). Results in other bands were comparable (see below, Results). The specific calculation was as follows:

$$\text{Coherence}_{GC\leftrightarrow BLA}(f) = \left| \frac{1}{N} \sum_{n=1}^{N} e^{-i\left(\theta_t^{\text{GC}}(f) - \theta_t^{\text{BLA}}(f)\right)} \right|,$$

where $\theta_t^{GC}(f)$ and $\theta_t^{BLA}(f)$ are the GC and BLA LFP phases for time t and frequency f, and n is the counter for number of trials.

The error term for the evaluation of coherence magnitude was estimated using bootstrapping by resampling trials with replacement from individual recordings (500 such resamples were performed for each recording). Changes in taste-induced coherence were determined relative to baseline. The 750–250 ms period before stimulus delivery was selected as baseline, with time points closer to stimulus delivery ignored to avoid temporal bleed of coherence between prestimulus and poststimulus periods because of the slow frequencies considered here. If the mean value of the coherence during taste responses fell outside the 95% CI of the baseline period (see above), the deviation was deemed significant. The fraction of recordings with significant deviations were summed at each time point and across all recordings, enabling an estimation of the aggregate dynamics of these changes, and the resultant time series were smoothed (to remove brief, spurious deflections) using a second-order Savitzky–Golay filter with a 101 ms kernel (Press and Teukolsky, 1990). To visualize the dynamics of this phase coherence, changes in coherence from baseline were calculated for 4–7, 7–12, 12–30, 30–70, and 70–100 Hz, smoothed as above, and projected into three-dimensional space using principal component analysis implemented in scikit-learn software (Pedregosa et al., 2011).

A trial-shuffled control was used to test whether calculated phase coherence reflected a default similarity in BLA and GC LFP, that is, to test whether there were similarities between the regions on single trials above and beyond those visible in trial-averaged presentations. Essentially, the same phase-coherence calculations as above were performed on data for which trial order was shuffled between the pair of channels being compared. Differences between datasets (inter-region, intra-region, and shuffle) were then evaluated using the repeated measures ANOVA implemented in the Pingouin package (Vallat, 2018), with Comparison type and Frequency Band as factors, followed by pairwise Mann–Whitney U tests for *post hoc* analysis.

Analysis of spiking activity

Single-unit isolation

Spikes from electrophysiological recordings were sorted and analyzed offline using in-house Python scripts (https://github.com/abuzarmahmood/blech_clust). Putative single-neuron waveforms with >3:1 signal-to-noise ratio were sorted using a semiautomated algorithm. Recorded voltage data were filtered between 300 and 3000 Hz, grouped into potential clusters by a Gaussian Mixture Models fit to multiple waveform features; clusters were then labeled and/or refined manually (to increase conservatism) by the experimenters (Mukherjee et al., 2017).

Single-unit-evoked response characterization

Evaluating single-neuron response taste specificity. To statistically determine the degree to which the response of a single neuron contained taste-specific information, firing rates were estimated by binning spikes using rectangular rolling windows (length, 250 ms; step, 25 ms). A one-way ANOVA (between tastes) was then run on each window to identify whether the response of a single neuron to one taste was different from its responses to any other tastes at that time point; as the ANOVA was run separately for each time bin, and trials of different conditions (i.e., tastes) were separated by tens of seconds and randomized in order, the assumption of data independence (to which the analysis is fairly robust) was not inappropriately held. To lessen the likelihood of misidentifying random noise from true responses, a time bin was deemed to have significantly discriminative responses if it was part of three consecutive time bins with a p value < 0.05.

Evaluating single-neuron response palatability relatedness. To statistically determine the degree to which the response of a single neuron reflected the hedonic value of the stimuli delivered, we smoothed firing rates as described above and calculated the Pearson's correlation coefficient between the evoked firing rates and the palatability ranks of the tastants. Palatability ranks [sucrose (1) > NaCl (2) > citric acid (3) > quinine (4)], directly reflected consumption of (earlier-run squads of) rats in a Brief Access Task (see Sadacca et al., 2012). This ordering is canonical and has been replicated in many studies and with multiple measures of stimulus appreciation (Travers and Norgren, 1986; Clarke and Ossenkopp, 1998; Fontanini and Katz, 2006). Again, we reduced the likelihood of spurious positives in the noisy time series of neural firing by deeming neural responses to be significantly correlated with palatability only if the calculated correlation reached a p value of < 0.05 for three consecutive time bins.

BLA–GC spike count correlation

We extracted paired time series of spike counts across the 0–2000 ms poststimulus delivery for each trial. First-order differencing was performed on these time series to mitigate effects of serial correlations, after which the data were standardized using z-scoring. Correlations between the spike trains, and corresponding p values, were calculated using the Scipy implementation of Spearman's ρ (Virtanen et al., 2020). To aggregate comparisons within a single recording, the fraction of correlations achieving significance across all combinations of inter-region neuron pairs (for a single recording session) was calculated. As a control, this same fraction of significant correlations was calculated for 4000 trial-shuffled comparisons for each dataset to generate bounds on the fraction of significant correlations expected by chance. If the value for the fraction of significant correlations present in the actual data was beyond the 95% percentile for the corresponding shuffle distribution, the value was deemed significant.

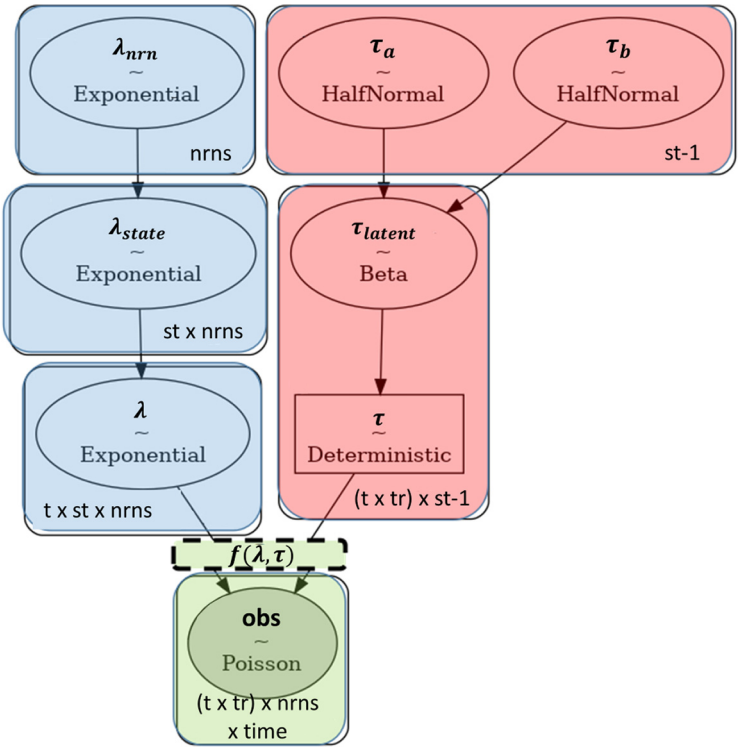

Figure 1. Dependencies between the random variables for constructing the changepoint model. Different colors denote different parts of the model; blue, emission variables; red, changepoint position variables; green, likelihood. Numbers on top left of each module in the rectangle correspond to the variable (equation) each module represents. Numbers on bottom right of each module correspond to the shape of the variables (and match with the shapes defined in the equations above). nrns, Neurons; st, states; t, tastes; tr, trials; time, time bins.

Changepoint modeling of population activity

Model fitting for GC. GC ensemble taste responses have been repeatedly shown to involve sudden, coherent firing-rate transitions. Because these transitions typically involve firing-rate changes in ~50% of the neurons in simultaneously recorded ensembles (Jones et al., 2007), and because they are sudden and stark (see below), they can be observed in single trials using any of a number of methods (see Mukherjee et al., 2019) and can be robustly inferred from ensembles as small as six neurons (Jones et al., 2007). Here, a multi-changepoint model written in the probabilistic programming language pymc3 (Salvatier et al., 2016) was used to determine the presence and latency of changes in ensemble responses.

It is important to note the uncertainty inherent in measuring the latency (and hence duration) of these transitions between hidden states using point process data (spike trains). This uncertainty is a function of the magnitude of firing-rate changes, the noisiness of the spike trains themselves, and the number of simultaneously recorded neurons. Taking these constraints into account, previous work (Sadacca et al., 2016) has shown that the durations of transitions in recorded data are statistically indistinguishable from those observed using simulated data for which the underlying transition was by design instantaneous, that is, for which the firing rates of simulated spike trains changed instantaneously at state transitions. (Note that the latency of these transitions was taken from analysis of experimental data, and therefore the simulations generated spike trains with peristimulus time histograms (PSTHs) identical to those in the real data.) Such analyses allow us to confidently conclude that the transitions detected in actual data (although they might appear longer because of noisy inference) likely correspond to instantaneous changes in the underlying firing rates of the neurons.

A detailed explanation of the changepoint model structure and code used to identify ensemble transition times can be found online at https://github.com/abuzarmahmood/pytau/blob/development/pytau/examples/Bayesian_Changepoint_Model.ipynb. Briefly, taste-evoked spike trains (the 2000 ms after stimulus delivery) were binned into 50 ms bins. Poisson likelihood was used to model the binned spike counts. The model is broken down, similar to a hidden Markov model (HMM), into two sets of latent variables, (1) the emission variables (i.e., firing rates) and (2) the changepoint position variables (i.e., when changepoints occur).

The response of a single-neuron to different tastes will be more similar than the responses of different neurons (even to the same taste). Equations for the emission variables below hierarchically model firing rates (emissions) to exploit this similarity such that the mean activity of each neuron is modeled independently (λ_{nrn}); emissions for each state and neuron (λ_{state}) are dependent on λ_{nrn}; and emissions for each taste, state, and neuron (λ) are dependent on λ_{state}. This results in values of λ being drawn from a distribution of λ_{state} values, which in turn are drawn from distributions of λ_{nrn} values. This organization better constrains the space of emission values during different states for each neuron (i.e., the model knows the emission for State 1 for Neuron 1 will be similar to State 2 for the same neuron), allowing the model to fit more robustly. The changepoint positions are defined assuming that the distribution of hyperparameters (τ_a, τ_b) for a changepoint are shared across all trials for each given changepoint (e.g., hyperparameters for first transition is shared for the first transition across all trials, likewise the second transition, etc.) but different for different changepoints. Finally, the latent emissions and changepoints are combined to generate time series of firing rates with sequential states ($f(\lambda,\tau)$ is a deterministic function; https://github.com/abuzarmahmood/pytau/blob/development/pytau/examples/Bayesian_Changepoint_Model.ipynb shows exact implementation), which is used to evaluate the likelihood of the data given the latent variables (obs). The dependencies between the equations are visualized in Figure 1.

Emission variables are as follows:

$$\lambda_{nrn} \sim Exponential\,(\mu_i,\ shape = neurons) \quad \forall \mu_i = Mean\ firing\ for\ neuron_i$$

$$\lambda_{state} \sim Exponential\,(\lambda_{nrn},\ shape = states \times neurons)$$

$$\lambda \sim Exponential(\lambda_{state},\ shape = tastes \times states \times neurons)$$

Changepoint position variables are as follows:

$$\tau_a, \tau_b \sim Half\ Normal\,(3,\ shape = states - 1)$$

$$\tau_{latent} \sim Beta\left(\tau_a, \tau_b, shape = (tastes \times trials) \times states - 1\right)$$

$$\tau \sim Deterministic\left(\tau_{latent}, shape = (tastes \times trials) \times states - 1\right)$$

Likelihood as follows:

$$obs \sim Poisson(f(\lambda,\tau), shape = (tastes \times trials) \times neurons \times timebins)$$

$$Where\ f(\lambda,\tau) \mapsto \text{Firing rates}\,(shape = (tastes \times trials) \times neurons \times timebins).$$

A modularized pipeline was used to fit and analyze the models across datasets (https://github.com/abuzarmahmood/pytau/tree/development/pytau).

Model fitting for BLA. The same changepoint analyses described above were also brought to bear on BLA ensembles to test whether BLA population dynamics can be validly described, like those observed in GC, as transitioning suddenly and coherently. For these analyses, we

used a separate cohort of two rats (nine recording sessions in total) in which we performed bilateral BLA recordings to obtain larger neural populations (results were qualitatively similar for those obtained from BLA–GC dual-region recordings).

We compared goodness of fit for changepoint models fit to the recorded (actual) data with that for models fit to two surrogate datasets in which the single-trial coordination of the neural population was perturbed. To generate these surrogate datasets, we started with the actual observed spike train data, and either (1) randomly shuffled whole trials for single neurons (e.g., such that Trial 1 for one neuron was paired with Trial 4 for another neuron), or (2) shuffled individual spikes from one trial to the same time bin in another trial for the same neuron. Both of these shuffling processes create datasets for which single-neuron PSTHs remain identical to the original while disrupting any coherent changes in population activity present on single trials (see Fig. 4*A*).

Model fitting was performed using automatic differentiation variational inference (ADVI, Kucukelbir et al., 2016) capabilities present in the pymc3 package. The ADVI algorithm optimizes the Evidence Lower BOund (ELBO) of the model. The ELBO is a lower limit on the marginal likelihood of the model (Blei et al., 2017); it automatically penalizes more complex models (which necessarily provide better apparent fits because they have more free parameters), allowing for model comparisons similar to the various information criteria. The ELBO is an integral part of the model fitting procedure, which makes it convenient and efficient to use as a tool for performing model comparisons. Statistical significance of differences between ELBO values for the actual data and shuffle conditions were determined using the two-way repeated measures ANOVA (from Pingouin) with Model States and Shuffle type as factors.

Determining number of states. As a time series can be fit with a model containing an arbitrary number of states, we performed model comparison to determine the most parsimonious number of states to describe BLA taste ensemble activity (0–2000 ms poststimulus delivery). We fit models with 2–10 states to each BLA population and used the ELBO for model comparison. For each dataset, we ranked the different models using their respective ELBOs.

Comparing transition-aligned changes in recorded activity to those in smooth surrogate data. To supplement the above comparisons (and thereby further test and/or strengthen our conclusions), we compared the magnitude of firing-rate changes across inferred changepoints in the actual data to that in the two surrogate datasets described above. Given that these magnitude changes should be maximal only when changepoints are correctly identified at the ensemble level, that is, when all neurons in the ensemble change their rates simultaneously in the trial, we would expect that changes in both single-neuron and population activity would be greater across inferred changepoints for the actual data versus the shuffled datasets. After inferring changepoints for models with four states (this number of states was determined to provide the best fit to our data; see Fig. 4), we computed the average firing rate in 500 ms bins on either side of each changepoint, calculating the magnitude of change across the changepoint for both single neurons and of the whole neural population (analyzed as changes in an instantaneous-activity vector comprising all simultaneously recorded neurons in a session). To compare both the average magnitude and pervasiveness of differences between activity in the datasets (to enhance conservativeness by accounting for the few large outliers skewing average changes in magnitude), we calculated (1) the number of neurons for which, on average, the actual data had larger magnitude of change across the transitions; (2) the number of neural populations for which the actual data had a larger magnitude of change across the transition; (3) the fold change of magnitude in firing for single neurons (shuffled data/actual data); and (4) the fold change in magnitude of the population vector. The number of larger neural transitions was calculated by assessing which group (actual data, whole-trial shuffle, spike-trial shuffle) had the largest change in activity across the transition, for every transition; this produces ratios for which group the largest transition belonged to.

Testing for significance of the likelihood that transitions are larger in the recorded data than in control simulations (points 1 and 2 above) was conducted using a one-way ANOVA followed by Tukey's *post hoc* test. Hypothesis testing for differences in magnitude was performed using the Wilcoxon signed-rank test with Bonferroni's correction (points 3 and 4 above).

Coordination of BLA and GC transition times

To test our central hypothesis regarding the coupling of BLA and GC transitions in single trials, we assessed synchronization of transition times using simple correlative statistics.

Testing transition-time correlation as a coordination metric. To test the utility of this approach, we first performed pilot analyses on GC ensembles (which are known to transition suddenly) with higher counts of simultaneously recorded neurons ($n \geq 10$ neurons/population). We divided these ensembles into two populations randomly, repeating the splits 10 times/ensemble to avoid any issues related to selection of unrepresentative groups. Transition times were inferred independently for each half-ensemble (using techniques described above), after which the values for transition times in the two halves were correlated (Spearman's ρ). The significance of these correlations was tested as described for the BLA–GC inter-regional correlations below.

BLA–GC transition time synchronization. Coupling between BLA and GC transition times was assessed as described above. Transition times were inferred independently for simultaneously recorded GC and BLA ensembles. Statistical significance of each correlation was determined at the single-transition level and also by aggregating across all experimental recordings.

At the single-transition level, the correlation coefficient of each transition was compared with the distribution of coefficients calculated by trial shuffling the data (1000 shuffles per each correlation) and deemed strongly correlated if it was more highly correlated than 90% of the trial-shuffled datasets. To determine whether the correlations we see across all recordings and transitions are collectively (i.e., at the aggregate level) significant, we determined the fraction of strong correlations for all datasets and compared this number to the fraction expected from random data. The fraction of significant correlations for random data was generated using trial-shuffled data similar to the single-transition correlation comparison; however, in this case, shuffled data were generated up to the number of transitions present in the original data (creating a dataset of the same size as the actual dataset but with shuffled data). The fraction of significant correlations was counted for this shuffled dataset, and the process repeated was $\times 1000$ times. This provided us with a distribution for the fraction of significant correlations expected from random data, and the fraction present in the actual data compared with this shuffle distribution. The p values for transitions in the actual data were calculated using the percentile relative to this shuffle distribution. Values from actual data were deemed significantly different if they had $p < 0.05$ for one-tailed comparisons with Bonferroni's correction against the shuffled distribution. For completeness, this was followed up with a binomial test with $\alpha = 0.05$ (with Bonferroni's correction). The two tests gave identical results.

Investigating the relationship between changepoint uncertainty and transition correlation strength. As alluded to above, uncertainty in estimating the time point of transitions limits the calculated correlation strength of transitions across populations (thus causing potential underestimation of BLA–GC transition coupling). This uncertainty is an inevitable result of inferring state changes from noisy firing rates. Because we use a Bayesian model, we are able to quantify the uncertainty in a transition latency estimate in the form of the variance of the posterior distribution of the transition position (τ). To assess the degree to which this uncertainty in changepoint position had an impact on the calculated BLA–GC transition correlation strength, we used the trial-averaged variance of transition posterior distributions, summed across regions, as a proxy (η) for the uncertainty contribution from each neural population (BLA-GC, see below) as follows:

$$\eta_{jk} = \sum_{i=\mathrm{GC,BLA}} \overline{var}_{ijk},$$

where $\overline{var}$ = average variance of τ across trials, i = brain regions, j = transitions, and k = recording session.

Once calculated, η was then linearly regressed against its respective correlation coefficient to determine the strength of the relationship.

Table 1. Model parameters for simulated network

Parameter	Value	Notes
Connectivity matrix, W	$\begin{pmatrix} 1.2 & -0.5 & 0.5 & 0 \\ -1.5 & 1.9 & 0 & 1.2 \\ -1.1 & -0.6 & 0 & -0.8 \\ -1.5 & -1.3 & -0.8 & 0 \end{pmatrix}$	First two rows are connection strengths from GC, second two rows are connection strengths from BLA
Threshold vector, T	$\begin{pmatrix} -15 & -12 & 1 & 2 \end{pmatrix}$	First two values for GC units, second two for BLA units
Noise amplitude, σ^I	$0.6\,sec^{-0.5}$	$0.6/\sqrt{dt}$ when coded in simulation
Time constant, τ	$0.010\,sec$	10 ms is typical for many cells
Simulation time step, *dt*	$0.0001\,sec$	100-fold smaller than the time constant for accuracy

Significance of this relationship was determined using two-tailed Wald's test with *t* distribution.

Network model simulation

We instantiated a simple network simulation to test whether groups of neurons, which were by definition coupled, produce responses with the properties observed in our BLA-GC recordings. Conceptually, the model is a firing-rate model, containing four units, each representing an ensemble of similarly responsive mixed excitatory and inhibitory cells, with the mean rate of each group being the relevant variable. Units are connected first as pairs, with each pair representing one unit from GC and one unit from BLA. Within these cross-regional pairs, the connectivity is set up like that of an oscillator with strong self-excitation within one unit and cross-connections being excitation in one direction and feedback inhibition in the other. It happens that the pairs do not spontaneously oscillate, but oscillatory-like activity is produced by the uncorrelated background noise added to each unit. One of the pairs has stronger cross-connections and is closer to being an inherent oscillator than the other pair, resulting in greater coherence in the activities of one pair than the other. Finally, the connections from one pair to the other are inhibitory, such that activity of one pair suppresses the others and vice versa. Noise causes occasional spontaneous transitions between states, with each state consisting of one cross-regional pair of active units. For a graphical representation of the model structure, see Figure 10*A*.

Specifically, each model unit, *i*, has a firing rate, r_i, which responds linearly to its total input, I_i and varies according to the following:

$$\tau \frac{dr_i}{dt} = -r_i + I_i - T_i, r_i \geq 0,$$

where T_i is a threshold, indicating the minimum input needed for activity, or (if negative), its magnitude indicating the level of spontaneous activity in the absence of input. Importantly, as rates cannot be negative, we enforce $r_i \geq 0$ when the above dynamical equation would indicate otherwise. The input current to each unit is given by the weighted sum of connected units plus an independent white noise term as follows:

$$I_i(t) = \sum_i W_{ji} r_j(t) + \sigma^I \eta(t),$$

where σ^I is the SD of the noise, and $\eta(t)$ is an uncorrelated white noise term with zero mean and unit SD, $\langle \eta(t) \rangle = 0$ and $\langle \eta(t)\eta(t') \rangle = \delta(t - t')$.

Values of the parameters are shown in Table 1. Simulations were conducted in MATLAB (version R2018a) using the Euler–Mayamara method for integration. Code is freely available online at https://github.com/primon23/Two_State_Oscillators.

Phase coherence for network model

The simulation described above was used to generate 20 trials of neural activity. The activity of both units in each region was summed to produce a single time series that was treated as an analog for LFP. This LFP was then bandpass filtered (10–40 Hz) and subjected to a Hilbert transform, and instantaneous phase was estimated using the analytical signal from the transform. Because latencies of state transitions in the simulated activity are random (unlike experimental data, where they are roughly bounded in latency and occur in a sequential order, a fact likely related to the omission of the biological processes of the model with longer time constants, like synaptic depression/facilitation or firing-rate adaptation), we calculated phase coherence for the simulated data in each state using windows of activity centered around the transition from the more→less coherent state. Data across trials were aligned to state transitions from the more→less coherent states and snippets with radius = 350 ms (minimum duration of states across all trials) of the LFP phase were taken around the transition time. Intertrial phase coherence calculation was performed on these aligned snippets as described above.

Data Availability

We have structured our electrophysiology datasets in a hierarchical data format (HDF5) and are hosting the files on a university-wide network share managed by Library and Technology Services (LTS) at Brandeis University. These HDF5 files contain our electrophysiology recordings, sorted spikes, and single-neuron and population-level analyses (and associated plots and results). These files are prohibitively large to be hosted on a general-purpose file share platform; we request people who are interested in our datasets to contact the corresponding author, Donald Katz (dbkatz@brandeis.edu), who can put them in touch with LTS to create a guest account at Brandeis to securely access our datasets (hosted on the katz-lab share at files.brandeis.edu). Code to perform the network model simulations can be found at https://github.com/primon23/Two_State_Oscillators.

Results

To appropriately contextualize our novel central hypothesis and analysis, we build the following accounting of the results in a step-by-step manner. We start by replicating/confirming basic results from our prior work (Figs. 2, 3) and move on to testing basic questions concerning whether BLA responses show within-trial firing-rate transitions that could conceivably be coupled with those of GC (Figs 4, 5). From there, we move on to using field-standard techniques to test whether GC and BLA responses show simple trial-to-trial coherence (Fig. 6), and whether coherence changes from one response epoch to the next (Figs. 7, 8). Once epoch specificity of response coherence is established, we move on to testing whether BLA–GC coupling during taste processing is specifically instantiated in the synchrony of transitions into and out of the GC palatability-related epoch, and whether the entirety of these phenomena is truly consistent with the function of tightly coupled networks (Figs. 9, 10).

Simultaneous single-neuron ensemble recordings from BLA and GC

We isolated multiple single neurons simultaneously from both GC and BLA in six rats. Electrode bundle tip placements are shown in Figure 2; a coronal schematic of the regions (GC, Fig. 2*Ai*; BLA Fig. 2*Bi*), with the locations of all bundle tips marked,

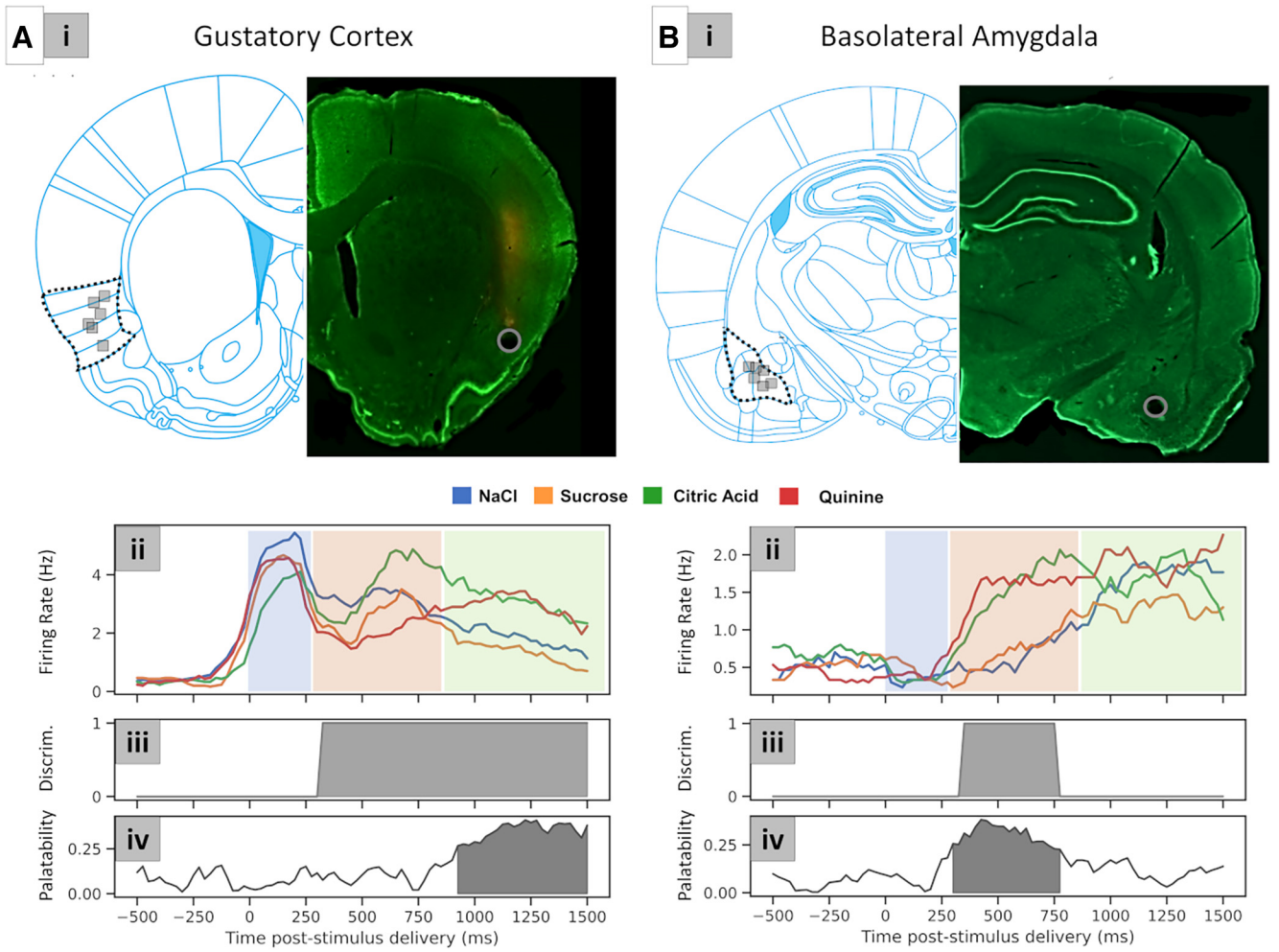

Figure 2. Histology and example PSTHs from recorded regions. ***A, B,*** GC (***A***), BLA (***B***). Schematics and sample histology (2× magnification) showing electrode bundle placements. Brain slices were registered to brain atlas schematics at 1.4 mm anterior to bregma for GC and 3.00 mm posterior to bregma for BLA. Dashed lines outline GC and BLA, with gray squares showing the final locations of each electrode bundle. Gray circles in the photomicrographs outline electrolytic lesions (schematics were modified from Paxinos, 2007) (***Ai,Bi***). PSTHs for representative GC and BLA single-neuron responses to each taste. Previously described response epochs (Katz et al., 2001) are denoted with different colored shading behind the PSTHs (***Aii,Bii***). Boolean time series reflecting whether neural activity significantly differentiates tastants (0 = no, 1 = yes) at a particular time point, with shading emphasizing periods of significant differences among responses (***Aiii,Biii***). Correlation of neural activity with taste palatability (see above, Materials and Methods) through time; shaded regions denote periods of significant correlation (***Aiv,Biv***).

is displayed on the left half. The right half is a photomicrograph showing an example placement.

The rest of Figure 2 presents representative recordings from each region. Figure 2, *Aii* and *Bii*, shows overlain PSTHs of example GC and BLA neuron responses to each taste. The colors behind the PSTHs show the average periods of GC coding epochs described previously (Katz et al., 2001; Fontanini et al., 2009; Sadacca et al., 2012). Note that both GC and BLA responses rearrange themselves (i.e., the ordering of which tastes induce larger/smaller response magnitudes changes, *y*-axis) around the times of epochal boundaries. The nature of the coding performed by each neuron changes with these epochal rearrangements as well (Katz et al., 2001; Sadacca et al., 2012, 2016; Moran and Katz, 2014; Li et al., 2016). In GC, the early epoch has little taste specificity, but the middle epoch responses code at least a subset of tastes distinctly, and in the late epoch, responses become generally organized by palatability. (Note, for instance, in Figure 2*Aii* that the late response is ordered from most aversive to most palatable; the strongest response is to quinine, followed in order by citric acid, NaCl, and sucrose.) In BLA, meanwhile, palatability-related responses appear in the middle epoch, and (unlike the GC responses) primarily reflect strong responses to tastes of only one (in this case, negative) valence; both of these aspects of BLA taste responses replicate previous investigations (Fontanini et al., 2009).

These findings are statistically confirmed by analyses summarized below the PSTHs in Figure 2. The middle row (Discrim in the *y*-axis; Figure 2*Aiii*,*Biii*), which plots the significance ($p < 0.05$) of a moving window of ANOVAs for tastes, reveals that the responses displayed in Figure 2*A–Bii* become distinctly taste specific starting at ~250 ms after taste delivery (i.e., at the start of the second epoch; the BLA neuron stops doing so at the end of this epoch). At the bottom (Fig. 2*Aiv*,*Biv*), Pearson's *r* between the known palatability of each taste and the response of the neuron to each taste (shaded region, $p < 0.05$) shows that the palatability relatedness of the GC responses becomes significant a little before 1000 ms after taste delivery [i.e., at the onset of the third (late) epoch], and that the palatability relatedness of the BLA responses is significant for the one-epoch entirety (middle epoch) of the taste-specific response. Again, these results confirm findings published in multiple previous studies (Katz et al., 2001; Grossman et al., 2008; Fontanini et al., 2009; Sadacca et al.,

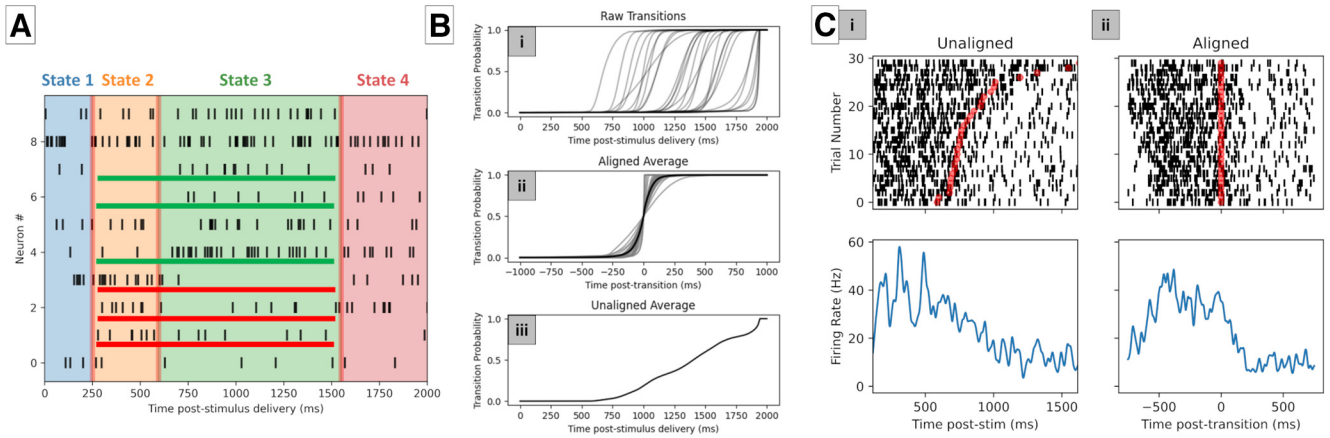

Figure 3. GC-evoked population activity contains sudden state transitions. ***A***, A single trial of GC taste-evoked activity in 10 simultaneously recorded single neurons. Inferred states (here identified using an ensemble changepoint algorithm) are indicated in overlain shading. For the transition leading into the period of palatability-related activity (i.e., from State 2⟶State 3), spike trains that increased in firing rate are underlined in green, and spike trains that decreased in firing rate are underlined in red. ***Bi–iii***, Identified time courses for the State 2⟶3 transition in 30 trials for a single ensemble (***i***). Aligning the middle (i.e., 0.5 probability) of the transitions shows that they typically occur suddenly (***ii***). When averaged across data synchronized to stimulus onset, however, the transition appears smooth and slow (similar to neural activity in trial-averaged PSTHs, ***iii***). ***Ci,ii***, The raster plot (above) and PSTH (below) for a single representative GC neuron that shows a sudden decrease in its firing rate occurring at variable latencies across trial. The time of the transition, inferred by the changepoint algorithm on activity of the entire simultaneously recorded ensemble is shown with a red circles (***Ci,Cii***). By aligning activity to calculated transition times (producing a peritransition time histogram), the sharp decrease in neural activity across the transition can be better appreciated (***ii***).

2012) and motivate our basic hypothesis that the systems-level mechanisms of taste coding will intrinsically involve epoch-specific processes.

A good deal of previous research has demonstrated that taste-response epochs translate into sequences of states (each lasting hundreds of milliseconds) in single-trial-evoked GC ensemble activity (Jones et al., 2007; Sadacca et al., 2016; Mukherjee et al., 2019), with each pair of states separated by sudden (50–200 ms) coherent firing-rate transitions (spontaneous GC activity also contains such transitions; Mazzucato et al., 2015; La Camera et al., 2019). We note here that we use the term "epoch" to describe periods of distinct activity seen in single-neuron PSTHs (Fig. 2), whereas "state" is a term borrowed from the modeling literature and is used here to describe simultaneous changes in the recorded neural population activity while accounting for temporal variation at the single-trial level. However, as state transitions correspond to epoch transitions across trials (on average; Fig. 9*C*,*D*, comparison of average state-transition times in our data and previously shown epochal-transition times), it is sometimes difficult to cleanly delineate single-trial from trial-averaged analyses. In these cases, we use the term that seems most appropriate.

These state transitions represent an integral part of neural activity, in that they both predict the onset of (Sadacca et al., 2016) and drive (Mukherjee et al., 2019) consumption-related behavior; that is, rather than being trivial reflections of mouth movements, the dynamics represent the processing of tastes that leads to discriminative mouth movements (Katz et al., 2001; Jones et al., 2007). The seeming ramping onset of the late epoch containing palatability-related firing (Figure 2) described above is an artifact of averaging across the large trial-to-trial variability (on the order of hundreds of milliseconds) in the latency of this sudden transition (Jones et al., 2007; Sadacca et al., 2016). Furthermore, because this phenomenon is not sparse, (~50% of the neurons in an ensemble will change their firing rates at any particular transition), it can be reliably observed in subensembles as small as six simultaneously recorded neurons (Jones et al., 2007).

Once again, the current data replicate these findings (Fig. 3), showing that even a small ensemble of simultaneously recorded GC neurons (here, 10; again, almost two times the number of neurons needed to resolve this phenomenon; Jones et al., 2007) can be observed to undergo sudden, coherent firing-rate changes in the process of responding to tastes (Fig. 3*A*). The states and state transitions identified by our changepoint algorithm are overlain on the ensemble raster plot, and the six (of 10, 60%) neurons that significantly increased or decreased their firing rates at the time of the transition into the third (putative palatability related) state are indicated with green or red lines, respectively, under their spike trains. (Note the sudden increase in the rate of spiking in neurons 4, 6, and 7, and the simultaneous decrease in firing rate in neurons 1, 2, and 3.) The algorithm was able to progress to near-perfect confidence in the transition across an extremely short time interval in almost every trial (Fig. 3*Bi*), which is to say that these changes in neural activity are, on average, very sudden on a single-trial basis (Fig. 3*Bii*); because the latency of the transition could vary wildly from trial to trial (Fig. 3*Bi*), however, the onset of the post-transition state appears to be slow-ramping when averaged across trials synchronized to stimulus delivery (Fig. 3*Biii*).

Once calculated from the ensemble data, the time of transitions could then be used to directly illustrate the sharpness of the firing-rate changes in even single-neuron data. Figure 3*C* shows a representative GC neuron; note that the firing-rate change that seems like a slow ramp in data synchronized to stimulus delivery (Fig. 3*C*, top, unaligned rasters; bottom, associated peristimulus time histograms) is in fact precipitous when the trial-to-trial variability of the latency of that change is accounted for (Fig. 3*Cii*, aligned raster and associated peritransition time histogram). Keep in mind that this change is not caused by the stimulus being removed from the tongue; it occurs at least a full second before swallowing and both precedes and reliably predicts (Sadacca et al., 2016), as well as participates in, driving (Mukherjee et al., 2019) discriminative oral behaviors.

BLA activity contains trial-specific, sudden ensemble firing-rate transitions

Having reconfirmed that GC epochal dynamics reflect sequences of single-trial states and are en route to assessing the coordination between BLA and GC neural responses and testing our

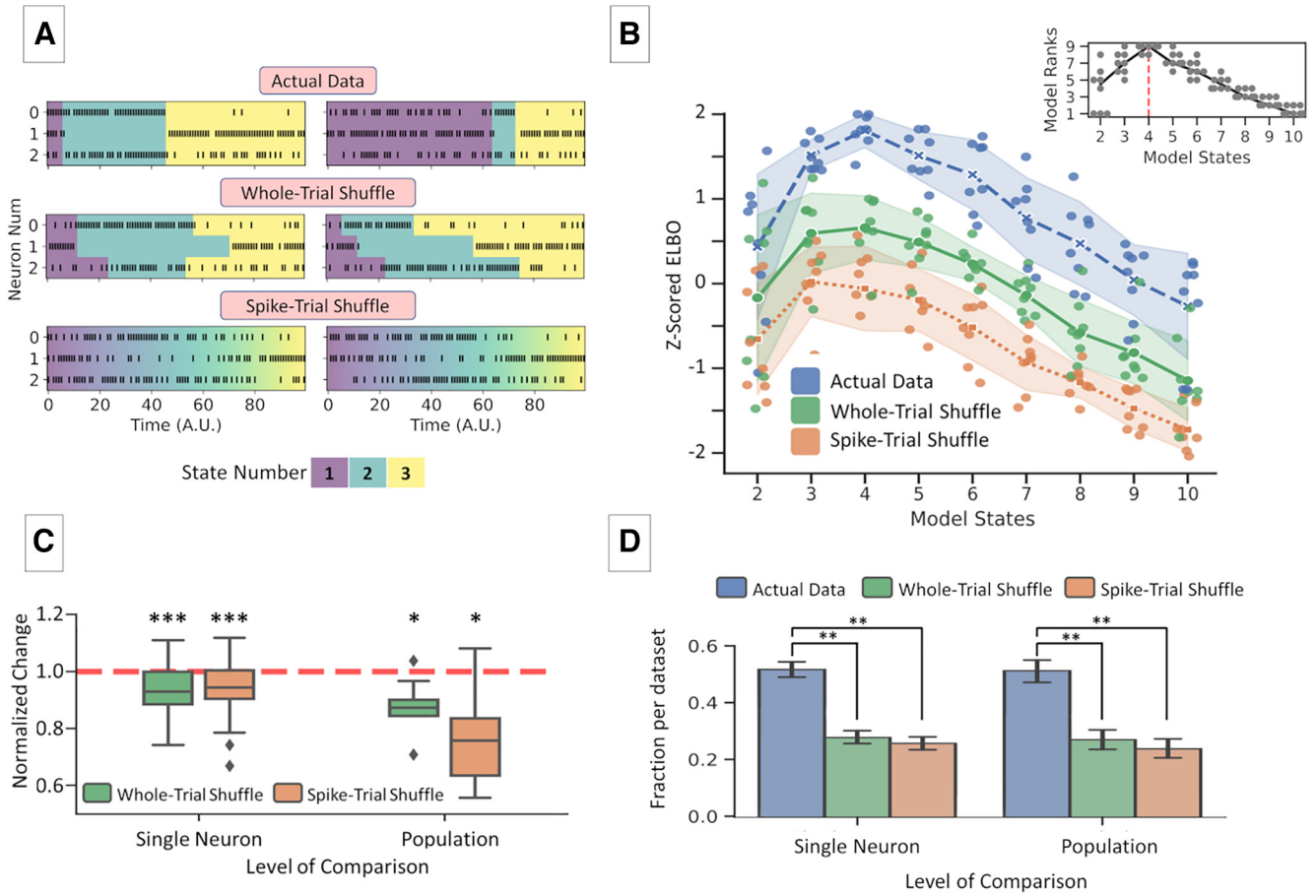

Figure 4. BLA population responses can validly be characterized as progressing through a sequence of state transitions. ***A***, Visualization of how the actual data were transformed by the different shuffling procedures. Raster plots are overlayed with colors identifying states for the neural population; two trials (one in each column) are shown. *Actual Data*: state transitions are hypothesized to occur coherently across all neurons for the same trial. *Whole-trial shuffle*: state transitions are mismatched between neurons on the same trial. *Spike-trial shuffle*: sharp, trial-variable state transitions have been destroyed by changing in which trial each particular spike occurred, largely leaving smooth changes in the neural activity, which are consistent across trials. A.U., Arbitrary units. ***B***, ELBO values for 2–10 state models fit to the actual data and surrogate datasets. Note that the ELBO (unlike model likelihoods) penalizes more complicated models, allowing us to visualize peak fit rather than seeking an actual elbow in monotonically increasing functions. Inset, Ranks for models with 2–10 states. Models with four states consistently show the highest ranks across the dataset. Solid black line shows median rank per state. ***C***, Comparison of average, normalized changes in single-neuron and population vector firing rates in the vicinity (from 500 ms before to 500 ms after) of transitions. Firing-rate changes across transitions are consistently diminished by shuffling, a decrement that is particularly noticeable at the population level. Edges of boxes show first and third quartiles, and the horizontal line through the boxes shows the median. The dashed red line denotes the (normalized) firing-rate changes in the actual data; $^{*}p < 0.05$, $^{***}p < 0.001$ for mean value is different from 1.0. ***D***, Comparison between actual data and shuffled surrogate datasets for which dataset contained the higher number of larger transitions. Unperturbed BLA datasets consistently had more transitions with largest changes in firing rate (mean ± SEM; $^{**}p < 0.01$).

Table 2. Statistical tests for results in Fig. 4*B*

One-way Repeated Measures ANOVA (between States = 3,4,5, $n = 9$ BLA populations)	
$F(2,16) = 7.138$, $p = 0.007$	
Wilcoxon Signed-Rank Tests with Holm's Correction, $n = 9$ BLA populations for each test	
Comparison	Statistics
States = 3 vs. 4	W-Statistic = 2.0, $p = 0.0469$
States = 4 vs. 5	W-Statistic = 1.0, $p = 0.0469$
States = 3 vs. 5	W-Statistic = 18.0, $p = 1.00$

Table 3. Statistical tests for results in Fig. 4*C*, Wilcoxon Signed-Rank tests

Level of comparison	Comparison	Statistics
Single Neuron ($n = 152$ single neurons)	Actual Data vs. Whole-Trial Shuffle	Statistic = 1989.5, $p = 5.65 \times 10^{-14}$
	Actual Data vs. Spike-Trial Shuffle	Statistic = 2321.0, $p = 3.76 \times 10^{-12}$
Population ($n = 9$ BLA populations)	Actual Data vs. Whole-Trial Shuffle	Statistic = 2.0, $p = 0.015$
	Actual Data vs. Spike-Trial Shuffle	Statistic = 2.0, $p = 0.015$

hypothesis that BLA state transitions are coupled to those in GC, it is necessary that we determine whether these sort of nonlinearities in firing rate, which have been extensively described in GC (Fig. 3; Jones et al., 2007; Sadacca et al., 2016), also truly characterize BLA taste responses. That is, we must first test whether evoked BLA activity, which involves epochal dynamics that are similarly timed to those in GC (Fig. 2, single-neuron examples of the similarity between BLA and GC dynamics; Fontanini et al., 2009), are well described as sudden ensemble state transitions in single trials. Only if the population dynamics of BLA taste-evoked responses also consist of sudden transitions between a small number of ensemble states (a hypothesis that has not yet been tested) is our most novel hypothesis tenable.

To this end, we evaluated the spiking activity of BLA ensembles using the same changepoint model designed to detect coherent ensemble transitions in GC data. To ensure robust sampling of BLA population activity, this set of analyses was performed on data from a separate group of animals with bilateral BLA

Table 4. Statistical tests for results in Fig. 4*D*

One-way ANOVA between Shuffle Type	
Level of comparison	Statistics
Single Neuron (n = 152 single neurons)	$F(2,316) = 117.2$, $p = 8.41 \times 10^{-39}$
Population (n = 9 BLA populations)	$F(2,16) = 8.206$, $p = 0.0035$

Post-Hoc comparisons, Pairwise Tukey-HSD		
Level of comparison	Comparison	Statistics
Single Neuron, n = 152 single neurons	Actual Data vs. Whole-Trial Shuffle	Difference = 0.232, SE = 0.016, p = 0.001
	Actual Data vs. Spike-Trial Shuffle	Difference = 0.252, SE = 0.017, p = 0.001
Population, n = 9 BLA populations	Actual Data vs. Whole-Trial Shuffle	Difference = 0.315, SE = 0.073, p = 0.001
	Actual Data vs. Spike-Trial Shuffle	Difference = 0.236, SE = 0.075, p = 0.0058

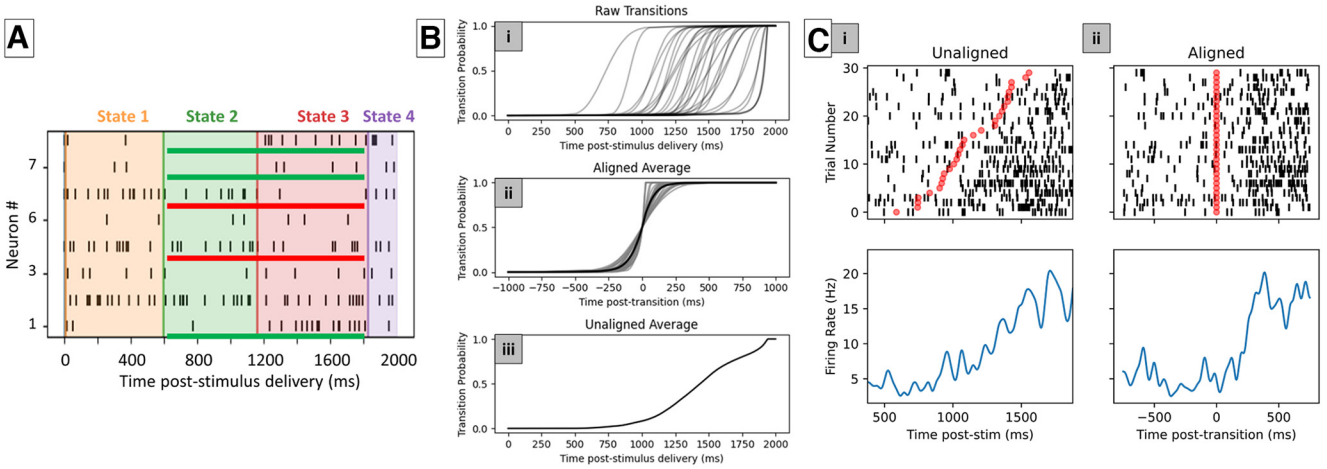

Figure 5. BLA-evoked population activity contains sudden state transitions. ***A***, A single trial of BLA taste-evoked activity in eight simultaneously recorded single neurons. Inferred states (here identified using an ensemble changepoint algorithm) are indicated in overlain shading. For the transition leading into the period of palatability-related activity (i.e., from State 2 to 3), spike trains that increased in firing rate are underlined in green, and spike trains that decreased in firing rate are underlined in red. ***Bi–iii***, Identified time courses for the State 2→3 transition in 30 trials for a single ensemble (***i***). Aligning the middle (i.e., 0.5 probability) of the transitions shows that they typically occur suddenly (***ii***). When averaged across data synchronized to stimulus onset, however, the transition appears smooth and slow (similar to neural activity in trial-averaged PSTHs, ***iii***). ***Ci–ii***, The raster plot (top) and PSTH (bottom) for a single representative BLA neuron that shows a sudden increase in its firing rate occurring at variable latencies across trial. The time of the transition, inferred by the changepoint algorithm on activity of the entire simultaneously recorded ensemble is shown with a red circles (***Ci,Cii***). By aligning activity to calculated transition times (producing a peritransition time histogram), the sharp increase in neural activity across the transition can be better appreciated (***ii***).

electrode implants (two animals, nine recording sessions; however, all results reported in this analysis were qualitatively similar to those obtained using unilateral BLA populations taken from BLA–GC dual region recordings; see below). First, we fit a battery of models containing 2–10 states to the evoked responses from the BLA ensembles and compared the goodness of fit of the probabilistic models (quantified using the ELBO; see above, Materials and Methods) with that of identical analyses performed on control datasets made by shuffling either whole trials or single spikes between trials for the same neuron (both manipulations preserve the across-trial dynamics and have equivalent PSTHs to the actual data; Fig. 4*A*). Performing this set of analyses allowed us to test whether the real data were better fit by the sudden transition model than one would expect by chance. We predicted that the unmanipulated data would achieve a higher goodness of fit to the sudden state change model.

This analysis revealed that models with four states had the highest ELBO, that is, that four-state models best describe BLA population activity for the 2000 ms of poststimulus activity we have used in this study (Fig. 4*B*, Table 2 for statistics used to test these effects). Note that only three of these states typically appeared in the first 1500 ms; that is, in the period leading up to and including the GC palatability-related state, and that while we are interested in the transition out of that palatability-related state, we are not yet prepared to interpret the state following (which is postdecision). This number of states accords well with results from HMM modeling of GC activity (Jones et al., 2006; Sadacca et al., 2016), supporting our suggestion that GC and BLA taste-response dynamics are similar in kind (and demonstrating that these results hold across very different analysis techniques). Furthermore, this fit was significantly higher (as was the relative advantage of the four-state model) than that achieved by even the trial-shuffled surrogate dataset ($F_{(2,20)} = 26.9$, $p = 2.13 \times 10^{-6}$; two-way repeated measures ANOVA for Shuffle type and number of States, n = 9 recordings across two animals), control data which left spike trains of each trial intact (Fig. 2), eliminating only the between-neuron coherence of single-trial dynamics.

We further evaluated the BLA ensemble data by comparing the magnitude of firing-rate changes across state transitions identified by this optimal four-state changepoint model (Sadacca et al., 2016, a similar analysis of GC responses), compared with those observed in surrogate datasets. We predicted that both the average magnitude of transition-aligned changes in firing rates and the quantity of transitions showing larger changes in firing

would be higher for the actual data than for the surrogate datasets in which we disrupted the coherence of single-trial changes in population activity. Our results confirmed these predictions; compared with the surrogate datasets, neurons and ensembles in the actual, unmanipulated BLA data showed consistently larger changes in firing rate across transitions (Fig. 4*C*, Table 3, an accounting of the extensive statistical analyses used in these tests). Furthermore, the percentage of BLA single neurons and ensembles for which changes in firing rate across transitions were largest in the actual data were more than twice that for either shuffled dataset (Fig. 4*D*; Table 4).

These findings suggest that BLA ensemble taste responses are well described as consisting of sudden, coherent firing-rate transitions in single trials. Figure 5*A* shows a representative ensemble taste response from eight simultaneously recorded BLA neurons that clearly involves rapid state transitions, one of which occurs at around the average time of GC transitions into palatability coding (Fig. 2). At this transition, five of eight neurons underwent either an increase or decrease of firing rate simultaneously (for another, neuron 3, the increase was almost but not quite significant). As in GC (Fig. 3; Jones et al., 2007; Sadacca et al., 2016), these transitions were variable in latency across trials (Fig. 5*Bi*), such that although the average transition time was brief (Fig. 5*Bii*), averaging across trials synchronized to stimulus delivery made that transition time appear artifactually slow (Fig. 5*Biii*).

Finally, we again fed back the results of this ensemble analysis to directly illustrate the sharpness of single-neuron firing changes across transitions. Figure 5*C* shows, for one representative BLA neuron, that firing-rate changes that seem like slow ramps in data synchronized to stimulus delivery (Figure 5*Ci*, unaligned raster and associated peristimulus time histogram) are in fact precipitous when the trial-to-trial variability of the latency of that change is accounted for (Fig. 5*Cii*, aligned raster and associated peritransition time histogram). Although we have no current explanation for the apparent slight delay in the firing rate change of this particular BLA neuron (we suspect that the answer lies in compromises made by the algorithm in settling on a best guess of transition time), it is clear that BLA ensembles, like GC ensembles, respond to tastes with sequences of states separated by sudden state transitions.

BLA and GC responses show strong trial-to-trial coherence

The above data motivate our hypothesis that taste processing involves BLA–GC coupling of the brief transitions into the state, which in GC, predicts and controls consumption behavior. But given that the vast majority of published studies assessing multiregion coordination have done so not in terms of momentary coupling—they have instead focused on multisecond responses with quantification performed via evaluation of the magnitude of correlation between spike counts in simultaneously recorded pairs of neurons (Averbeck et al., 2006a,b) or, alternatively, via evaluation of similarity in LFPs simultaneously recorded from the regions under investigation (Place et al., 2016)—we first assessed whether GC taste processing is coherent with that of BLA according to these standard metrics. To maximize our ability to compare our results to those of these earlier studies, we began our investigation of BLA–GC taste-response coupling by looking at these broader measures and then moved on (in the following sections) to testing the epochal specificity of this coherence, a result that would more directly motivate our ultimate test of the hypothesized synchronous BLA–GC transitions into the behaviorally relevant state.

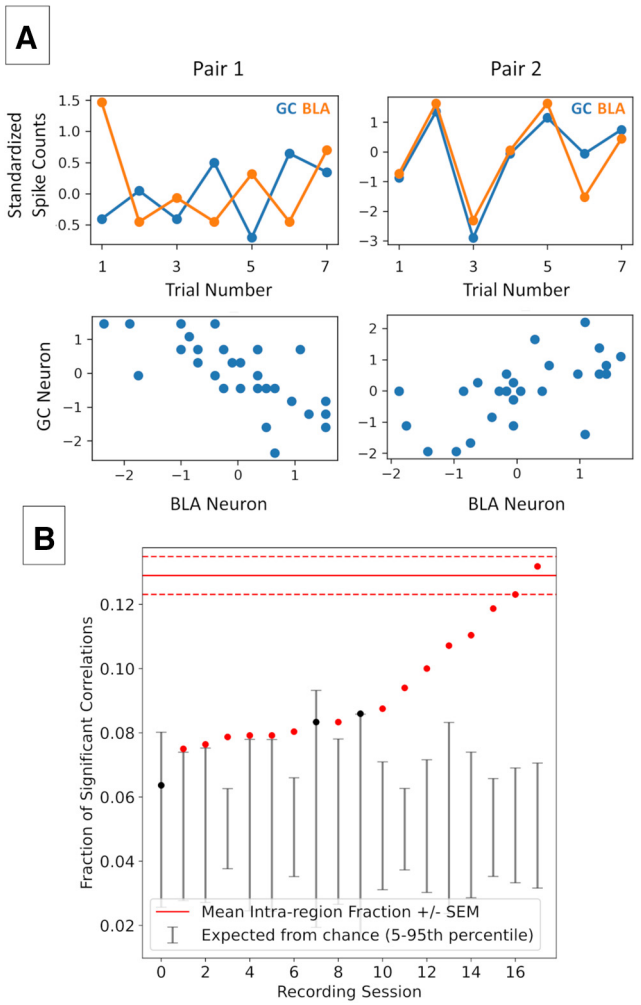

Figure 6. BLA and GC show strong spike-count correlations on a trial-matched basis. ***A***, Top row, Representative time series of (standardized) spike counts for two BLA–GC neuron pairs. Shown for each are consecutive sets of seven trials (of 30) showing negatively correlated (left) and positively correlated (right) activity. Bottom row, Same data as top row (but including all 30 trials) plotted as a scatter plot showing all the trials/pair; the negative (left) and positive (right) correlations in the scatter plot are easily seen. ***B***, A comparison of the fraction of significant correlations across all comparisons (neuron pairs × tastes) for trial-matched and trial-shuffled data (i.e., GC Trial 1 compared with BLA Trial 4, etc.). Trial-matched spike-count correlations (filled circles) are significantly higher in all but 3/18 sessions compared with the trial-shuffled comparisons (vertical lines); error bars show the 5–95th percentile interval of fraction of significant correlations per session expected by chance; red circles ($n = 15$) show sessions for which the fraction was higher than expected by chance, and black circles ($n = 3$) show sessions for which the value was within the chance interval. The interval marked by the horizontal dotted lines shows the mean ± SEM fraction of significant intraregion correlations (i.e., all BLA–BLA and GC–GC neuron pairs), included for reference.

We first considered the trial-wise strength of coordination between BLA and GC by investigating trial-to-trial spike-count correlations (using the 02–2000 ms poststimulus time period, which is the period of the most prominent taste-evoked response) for every simultaneously recorded BLA–GC pair of neurons, thereby testing the broad hypothesis that BLA and GC responses rise and fall in a correlated (or anticorrelated) manner from trial to trial. The two example GC–BLA neuron pairs shown in Figure 6*A* in fact demonstrate strong coherence on this time scale. The trial-to-trial firing rates of the pair on the left are (significantly) anticorrelated, a fact that can be particularly well appreciated in the scatter plot of BLA and GC firing rates (each dot

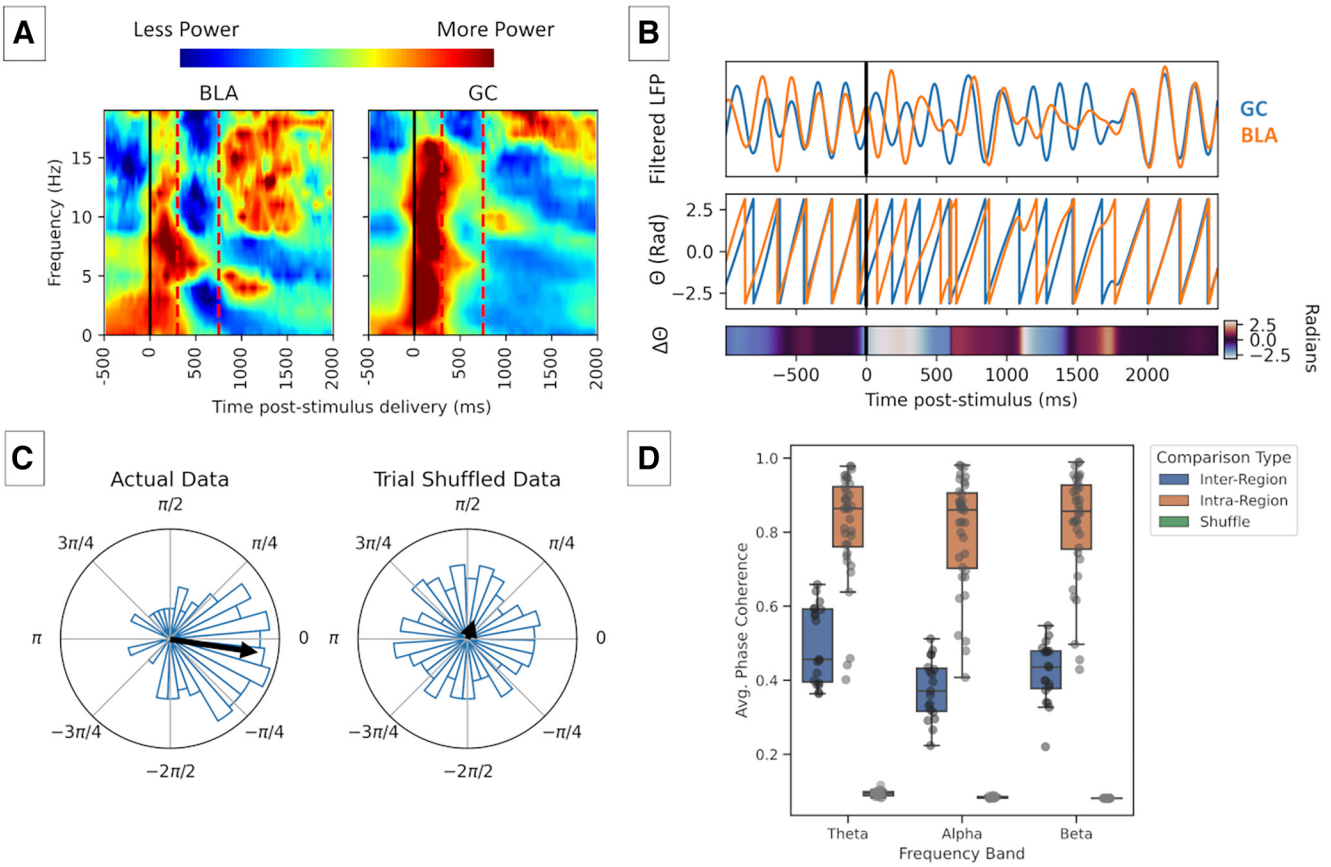

Figure 7. BLA- and GC-evoked LFP responses are similar on a trial-matched but not trial-shuffled basis. ***A***, Trial-averaged spectra of GC and BLA taste responses. Solid black lines mark taste delivery, and dashed red lines mark the average times of epoch onsets, which are well aligned with changes in the spectra in both regions. Power in each plot is *z*-scored by frequency for the time periods shown. ***B***, Calculation of BLA–GC phase difference for a single trial. Top, Filtered LFP (4–7 Hz) for each region; middle, extracted phase (Θ); bottom, phase difference (ΔΘ). ***C***. Phase difference histograms (length of blue bars = frequency of occurrence) used to quantify similarity between GC and BLA LFP using average intertrial phase coherence. Small phase differences (indicated by strong peaks in the polar histogram close to 0) indicate strong coherence. This is quantified using the magnitude of mean phase difference vector (black arrows). Data show the distribution of phase differences for $t = 0$ ms poststimulus delivery for actual and trial-shuffled data. ***D***, Mean phase coherence for 0–2000 ms poststimulus delivery across frequency bands. The value of the trial-matched comparison is significantly higher than the trial-shuffled comparison, suggesting there are similarities in the activity of both regions that are not present in trial-averaged data.

reflects one trial) below the trial-to-trial chart of responses; the pair to the right is similarly (albeit in this case positively) correlated.

Across the entire sample, BLA–GC neuron pairs (averaged across all pairs in a single session) almost always showed higher spike-count correlations than did trial-shuffled data (Fig. 6; 15/18 comparisons had values significantly higher than those expected by chance, $n = 18$ sessions from 6 animals), confirming that the taste responses of simultaneously recorded BLA and GC single neurons are coupled in magnitude. Of course, either positive or negative correlations indicate connectivity at the single-neuron level as a neuron pair can have either an effective excitatory or inhibitory connection between them. Both connection types characterize projections connecting BLA and GC, and either can create coordinated dynamics between both regions (Haley et al., 2016; Fu et al., 2020).

The time courses of BLA and GC taste responses are coupled

The above analysis reveals a broad coordination in BLA–GC neural activity; that is, trial-to-trial differences in firing rates in BLA neurons, measured in stimulus-evoked responses separated by >20 s, predict trial-to-trial differences in firing rates in simultaneously recorded GC neurons. But this result falls short of revealing whether this amygdala-cortical coupling has anything specific to do with taste processing. It is possible that taste responses are simply riding on generally coupled excitability existing at long time scales, not unlike that detected in studies of resting-state network dynamics (Raichle, 2015; Seitzman et al., 2019). Given our proposal that a central feature of BLA–GC coherence is the specific coupling of state-to-state transitions, it is important to first test whether this interregional coherence is epoch specific.

We therefore moved next to examining coherence in the time courses of taste-evoked responses, using analyses of LFPs that have often been used for such purposes (Antzoulatos and Miller, 2016; Place et al., 2016; Saravani et al., 2019). Even casual scrutiny reveals what appear to be striking similarities in the (trial averaged) spectral power/amplitude of BLA and GC field potentials (Fig. 7*A*). Although the dominant frequencies differ between regions, in both regions the frequency spectra change repeatedly across the 1–1.5 s following stimulus delivery in a manner that is well aligned with the approximate average timing of epochal transitions of ensemble firing described previously (Fig. 2; Katz et al., 2001; Fontanini et al., 2009; Sadacca et al., 2012).

These observations were statistically evaluated using quantification of the intertrial phase coherence (Stitt et al., 2017; Engel et al., 2020; Kramer and Eden, 2020; Zareian et al., 2020) between BLA and GC taste responses. Briefly, phase information for BLA and GC LFPs (across the 4–30 Hz band) was extracted using the Short-time Fourier transform, after which phase differences

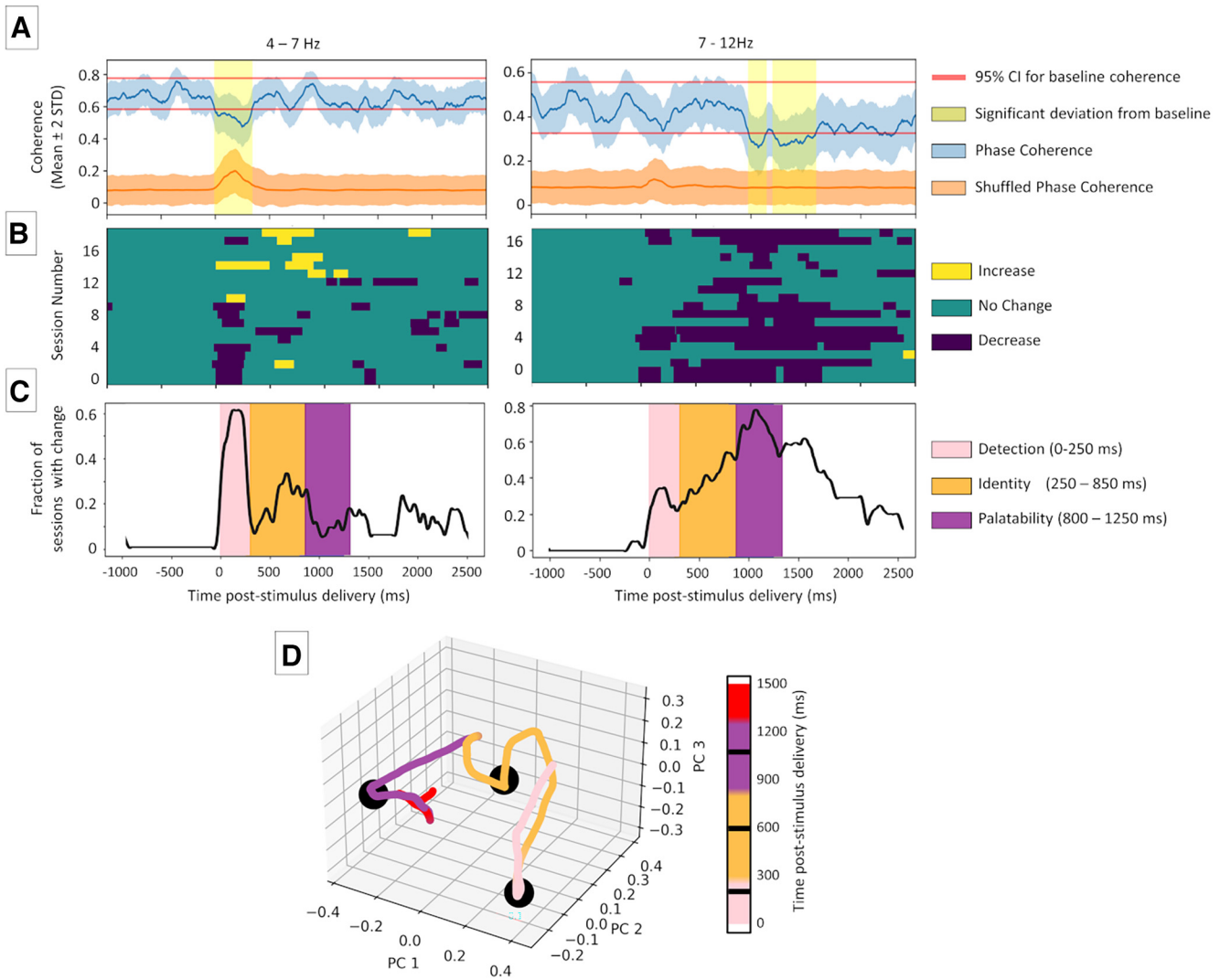

Figure 8. BLA–GC LFP phase coherence shows epoch-locked dynamics. ***A***, Representative examples of phase coherence in the 4-7 Hz (θ, left) and 7–12 Hz (μ, right) bands. Red lines denote the 95% confidence intervals determined by baseline coherence (−750 to −250 ms relative to stimulus delivery), and the yellow shading marks time points at which mean coherence changed significantly from that baseline. ***B***, Time points and directionality of changes in phase coherence relative to baseline for all sessions. Although changes in the 4–7 Hz band show both increases and decreases (Note that the most prominent changes from baseline, which are found in the earliest aspects of the responses, mostly consist of reductions of coherence.), changes in the 7–12 Hz band consist entirely of decreases in coherence. ***C***, The fraction of recordings in which phase coherence deviated from baseline. Bands correspond to those of the plots above them. Note that the time points of changes in coherence relative to baseline match strongly with timings of the canonical taste epochs (noted with overlain shading). ***D***, PCA projection of changes in phase coherence (as in ***C***) for 4–100 Hz. Black circles indicate corners in the trajectory, the timings of which roughly correspond to each epoch (black ticks marks in color bar). Colors indicate durations of epochs (as in ***C***).

between the two regions were calculated (Fig. 7*B*). These measurements were aggregated across all trials for each time bin separately, and the variance was evaluated across poststimulus time bins (Fig. 7*C*); the tighter the resulting phase-difference distribution, the stronger the coupling. The results of this analysis revealed that although interareal coherence (blue bars) was inevitably smaller than intra-areal coherence (tan bars), it was significantly larger than the (control) coherence between mismatched trials (Fig. 7*D*). (It is worth noting that this measurement likely underestimates the true cross-coherence, because any epoch-to-epoch differences will add to the variance and reduce the across-trial average. This result held for all the frequency bands that we assessed (theta, 4–7 Hz; mu, 8–12 Hz; beta, 13–25 Hz; $F_{(2,34)} = 654.5$, $p = 7.21 \times 10^{-28}$ for comparison type using repeated measures ANOVA; for all pairwise comparisons, $p = 1.61 \times 10^{-7}$, all p values are at the lower bound for numerical error; pairwise Mann–Whitney U tests, $n = 18$ recordings across six animals). Qualitatively similar results were observed for simple cross-correlations between LFP power spectra for BLA and GC (data not shown). The trial-averaged time courses of GC and BLA activity, as measured in evoked LFP activity, are coupled above and beyond overall magnitudes in a manner that looks, at first blush, to be related to epochal processing (Katz et al., 2001; Fontanini et al., 2009; Sadacca et al., 2012).

BLA and GC cross-coherence is epoch specific

Given the above, the fact that the different GC epochs have been shown to reflect distinct coding processes, and the likelihood that BLA is more integrally involved in the coding of palatability than taste identity (Piette et al., 2012; Lin et al., 2021), we hypothesized that, beyond the overall time courses being coupled, the cross-coherence between GC and BLA (evaluated in LFP time courses) would itself be epoch specific.

Our test of this hypothesis is summarized in Figure 8, which reveals that phase coherence between BLA and GC is in fact modulated in an epoch-specific (and, as it turns out, frequency-specific)

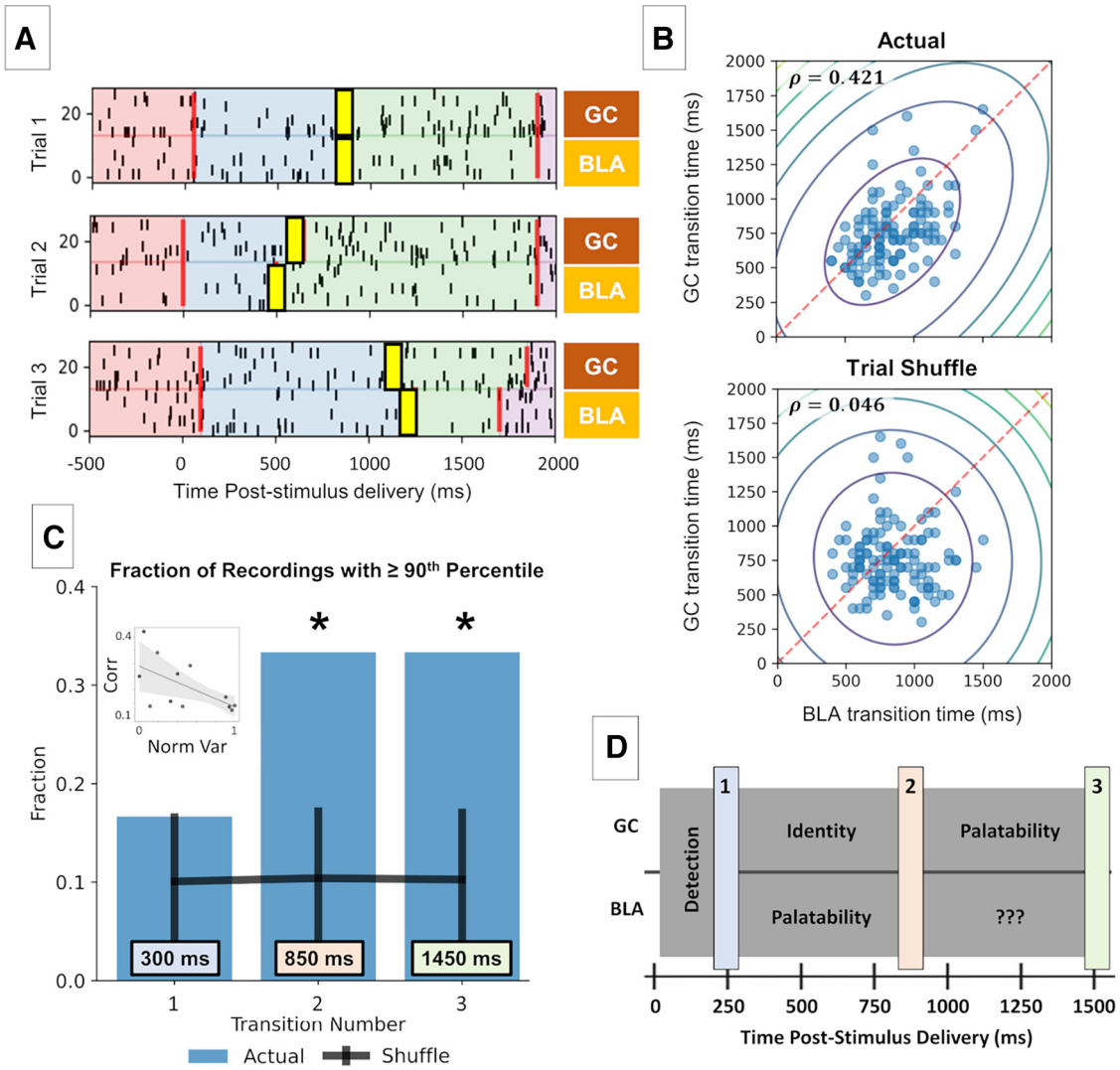

Figure 9. BLA- and GC-population-evoked responses involve coordinated state transitions. ***A***, Three representative trials highlighting the covariance of Transition 2 between BLA and GC. Transition 2 is highlighted with thick yellow lines. ***B***, The inferred times of GC state transitions plotted against those inferred for the simultaneously recorded BLA population for each trial of a representative transition; the scatter plot is overlain with contours of a 2D Gaussian around the data cloud. Top, actual data; bottom, trial-shuffled data; ρ = Spearman's correlation coefficient. ***C***, The fraction of datasets showing significant correlations for each transition (*$p < 0.05$). Blue bars represent the value in the actual data, and black lines indicate mean ± SD for fraction expected from random data. Only the fraction for Transitions 2 and 3 reached statistical significance. Colored boxes show average latency for each transition (poststimulus delivery). Inset, The variance (uncertainty) of transition latency distribution is significantly related to the correlation strength between BLA and GC transitions. Scatter plot shows correlation strength versus normalized variance of inferred transition posterior distribution. ***D***, The timings of the inferred transitions match well with the canonical epoch-onset times. Transitions 2 and 3 bookend the palatability epoch in GC (figure adapted from Fontanini et al., 2009).

manner by stimulus delivery. Changes in the theta (4–7 Hz) band were centered largely on the initial (i.e., taste nonspecific) epoch of the responses. In most (11/18) sessions, theta activity changed significantly from baseline; overwhelmingly (in 9/11 cases), these early response changes involved a decrease in phase coherence. In the mu band (7–11 Hz), meanwhile, changes were centered on the later (palatability specific; Katz et al., 2001; Sadacca et al., 2012) response epoch, These changes, which were even more ubiquitous than theta changes, in every case involved a decrease in coherence (Fig. 8*A*,*B*, right; $n = 18$ recordings across six animals). A reduction in coherence following stimulus delivery was predictable given previous results showing that strong levels of inter-region coherence tend to be associated with states of low cognitive engagement such as sedation, epilepsy, and cognitive impairment (Supp et al., 2011; Martinet et al., 2017; Arbab et al., 2018), as well as the fact that BLA and GC encode tastes nonidentically; hence, their specific neural responses are likely to differ (see below, Discussion). Note, however, that phase coherence always stays higher than random levels (BLA and GC are never functionally disconnected) and that state-specific reductions in coherence can be recapitulated in simple, tightly interconnected model networks (see below).

To aggregate these results across the entire dataset, we calculated the fraction of recordings in which coherence diverged significantly from baseline at each time point across the evoked response (Fig. 8*C*). These results confirmed the representativeness of the examples above, showing that 4–7 Hz coherence tends to be modulated early in the response and that 7–12 Hz coherence modulation comes on later in the response. Although we have no specific explanation for why theta coherence highlights an earlier epoch and mu a different epoch, what is clear is that BLA–GC coupling is modulated by epoch, as predicted.

To further illustrate the epoch specificity of BLA–GC functional connectivity, we subjected deviations of coherence from baseline across a broad range of frequency ranges (4–7, 7–12,

12–30, 30–70, and 70–100 Hz) to dimensionality reduction. In all bands we observed decrements in coherence, albeit with distinct temporal profiles (data for higher bands not shown). When we projected these time series of coherence deviation onto three principal components (Fig. 8*D*), the epoch-specific nature of BLA–GC coupling came into focus. The timing of sudden turning points in the trajectory, which are highlighted in Figure 8*D* using black circles, roughly correspond to the center points of the canonical epochs. Collectively, these data strongly recapitulate the epoch-wise nature of taste processing that has been recognized in GC and BLA spiking data, demonstrating that BLA–GC functional connectivity is not static and that BLA activity is explicitly tied to previously described GC dynamics (Lin et al., 2021).

BLA and GC ensembles undergo coupled state transitions

The structured dynamics of BLA–GC phase coherence suggests not only that BLA and GC population activity is coordinated but that this coordination is modulated according to the unfolding taste response. It further suggests that the trial-to-trial variability in amygdala-cortical dynamics might be coupled, providing indirect evidence for our riskiest hypothesis, which is that the sudden, behaviorally relevant transitions between ensemble firing-rate states (transitions that are a reliable facet of GC ensemble taste activity and that occur at different latencies in different trials) might be a distributed network phenomenon, coupled across GC–BLA ensembles. Such nonlinear coupling would suggest that BLA and GC behave as a distributed, yet single (putatively attractor), network, processing tastes in a unified manner in real time.

The analyses described in the above sections fall short of truly testing this hypothesis. In fact, they are strictly limited in their interpretability in this regard, specifically because population spiking changes in GC are quite sudden, and the latencies of these transitions vary by hundreds of milliseconds from trial to trial (Jones et al., 2006; Sadacca et al., 2016). These two properties of ensemble transitions ensure that any ability to evaluate their coupling will be essentially lost in across-trial averaging and obscured in moving-window analyses. Only through direct, single-trial analyses of the transitions themselves can we hope to evaluate BLA–GC coupling of such phenomena.

Given the novelty of this direct examination of inter-regional correlation of transition times, we first performed pilot analyses in which we divided datasets of simultaneously recorded GC neurons into halves, separately applied changepoint inference to each half-population, and correlated the latency of each transition between the two fits. We observed statistically significant correlations for >80% of our datasets and for each transition (n = 11 recordings; data not shown), confirming that our correlation measure is a robust metric for determining transition coupling between ensembles. Note that even these correlations were not significant for all datasets and did not reach ρ = 1.0 for reasons discussed below; see above, Materials and Methods.

We then brought this analysis to bear on simultaneously recorded BLA and GC ensembles, independently estimating transition times in each and then testing whether the latency of the first GC transition was correlated with the latency of the first BLA transition, and so on. The results of this test, which are summarized in Figure 9, demonstrate that certain transition times in BLA and GC ensembles are indeed robustly coordinated. Figure 9*A* presents one representative set of spike trains, showing inferred changepoints for a pair of simultaneously recorded BLA and GC ensembles and clearly revealing the close apposition of these transitions. Figure 9*B* (top) shows a scatter plot of independently calculated latencies of the second transition (the behaviorally relevant transition into palatability-related firing in GC; Sadacca et al., 2016; Mukherjee et al., 2019) from each of the trials for a representative session. Figure 9*B* (bottom) shows the scatter plot that would be expected by chance (produced after randomly shuffling a set of changepoint latencies between trials for the same dataset). The significant covariance between the GC and BLA changepoints on the top is lost with trial shuffling, proving that this transition alignment between the two regions is a within-trial phenomenon.

We statistically evaluated the strength of this BLA–GC transition coupling across the entire dataset by calculating the fraction of transitions that exceeded the 90th percentile of correlation strength relative to their respective trial-shuffled correlations (strongly correlated transitions) and statistically comparing this number to the fraction of strong correlations expected by chance for a similar-size dataset. This analysis revealed that the fraction of strongly correlated BLA and GC transition times in our data was significantly higher than those expected by chance but only for the transitions into and out of the GC palatability-related state (Fig. 9*C*; percentiles = 99.56 and 99.64, $p = 4.05 \times 10^{-3}$ and 3.65×10^{-3} for transitions 2 and 3, respectively; Bonferroni-corrected $\alpha = 0.05/3 = 16.67 \times 10^{-3}$; shuffle test with Bonferroni's correction, n = 18 recordings across six animals; see above, Materials and Methods).

Note that this evidence of significant coupling—the fact that the cloud of dots in Figure 9*B* (top) is elongated—is observed despite the relatively small ensembles of BLA neurons isolable in awake rats. It is quite likely that a good deal of the noise visible here reflects unavoidable noise in the estimation of transition time (see above, Materials and Methods). To test this suspicion, we calculated the relationship between the amount of uncertainty in the estimation of transition time of the model (i.e., the summed average variance of inferred transition distributions) and the strength of correlation between GC–BLA transitions. As suspected, we found a significantly negative relationship between the two variables (Fig. 9*C*, inset; slope = −2.3, r^2 = 0.352, p = 0.021, one-tailed Wald test for regression slope), a result consistent with the suggestion that uncertainty in the inference blurs the correlation between transitions. The strength of coordination between BLA and GC transitions is, thus, likely even stronger than that estimated here.

Note, however, that only transitions in and out of the state that have been previously shown to be related to the reaching of consumption decisions (Sadacca et al., 2016), namely, transitions that signaled the onset and offset of the palatability state in GC (Fig. 9*D*), were coupled across the BLA–GC network. Transitions from the GC Detection state into GC Identity state were not. This result dovetails nicely both with classic thinking about the specific role of BLA in emotional processing (Yamamoto, 2008; Baxter and Croxson, 2012) and with recent work from the lab that shows that optogenetic perturbation of the BLA→GC projection primarily affects GC processing during the palatability epoch in GC (Lin et al., 2021). Whereas BLA activity during the late epoch (Fig. 9*D*) has hitherto not been explored, the strong BLA–GC coupling during that time period recommends further investigation into processing performed by BLA during that time period. Together, these results suggest that the role of BLA–GC communication likely changes between epochs and even may only be important during the GC palatability epoch.

Modeling coupled state transitions with state-specific coherence

Together, the above results fill in a picture of BLA and GC as processing tastes as a single distributed unit, with significant (above chance) cross-coherence punctuated by coupled state transitions

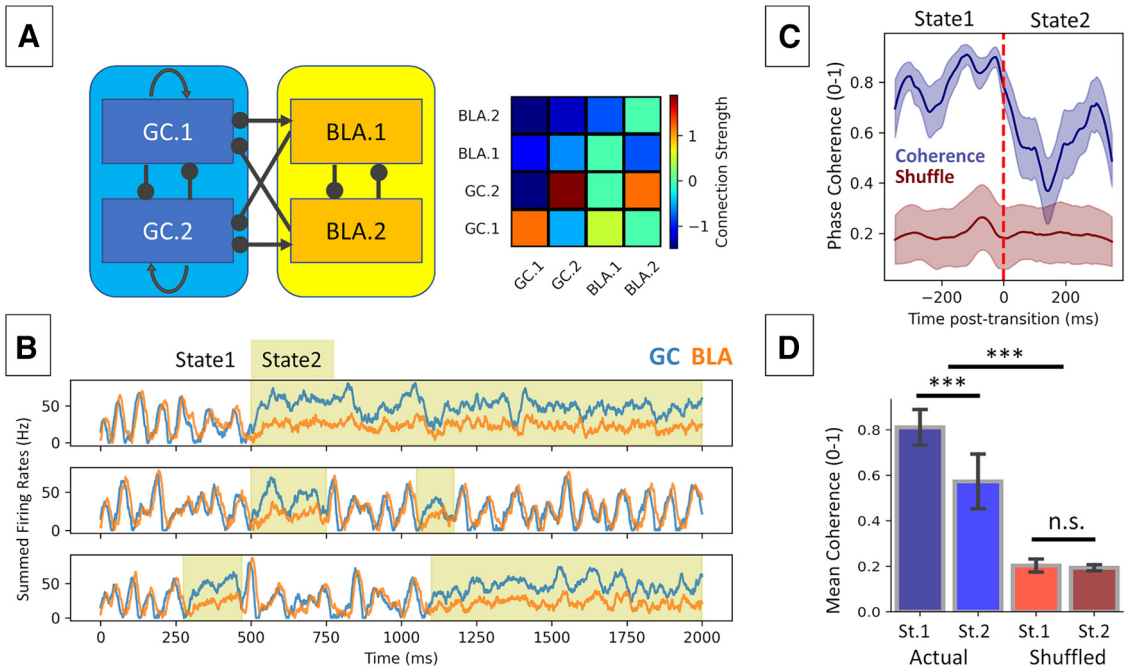

Figure 10. Coordinated state transitions and state-specific coherence in a coupled network model. ***A***, Network of four interconnected subpopulations that represent parts of GC and BLA. ***B***, Example trials showing activity of the network. Activity from both units in each region is summed as an analog of LFP. Highlighted regions marks time periods the system spends in the less coherent state (State 2). Note that both states have finite durations. ***C***, Intertrial phase coherence calculated on time windows 350 ms before and after transition from State 1→State 2 (more→less coherent state; mean ± SD). ***D***, Average coherence during each state (mean ± SD; St.1, State 1; St.2, State 2; ***= $p < 0.001$, n.s. = not significant).

across which the coherence drops in certain frequency ranges (a change indicative of intense processing). From a dynamical systems perspective, this phenomenology makes sense. Instantaneous coherence will often be state specific within a system in which state transitions are synchronized across brain regions; for just one example, brain regions collectively transition between different states of sleep; (Stitt et al., 2017). We would argue, in fact, that it is common for distributed networks of interconnected neurons to perform coupled transitions between states, some of which demonstrate decreases in LFP phase coherence.

We tested this contention by constructing a simple network model. Briefly, the network was composed of firing-rate units that can be taken to roughly represent interconnected subpopulations of BLA and GC neurons (Fig. 10*A*; right, connection strengths between subpopulations). When challenged with a moderate amount of input delivered to both regions (simulating either noise or taste stimulation, which initially arrives at BLA and GC via distinct paths; Gal-Ben-Ari and Rosenblum, 2012), the network enters a mode in which it switches between a more coherent state characterized by strong oscillations and a less coherent state where clear oscillations are disrupted (a switch that necessarily changes functional connectivity). Figure 10*B* presents the summed firing rates of simulated BLA and GC units across three trials in which the network can be seen to collectively transition between the states, one of which is clearly endowed with higher cross-coherence (State 1) than the other (State 2).

Figure 10*C* provides a specific analysis of these appearances, revealing that coherence indeed decreases following the transition into the less oscillatory state (State 2). In neither state, however, does this cross-coherence decline to baseline levels; the populations never fully disconnect (Fig; 10*C*,*D*; two-way ANOVA with State and Dataset, Actual vs Shuffle, as factors; State, $F_{(1)} = 184$, $p = 0.001$; Dataset, $F_{(3)} = 184$, $p = 0.001$; State * Dataset, $F_{(3)} = 233$, $p = 0.001$; Tukey's HSD *post hoc* tests, Actual State 1 vs State 2, $t = 42.7$, $p = 0.001$; Shuffle State 1 vs State 2, $t = 1.74$, $p = 0.302$). And although this network is admittedly simple (a fact that no doubt explains the simple, randomly timed back-and-forth between two states), it is not the only way that such a model can be constructed. Other versions can allow each region to intrinsically oscillate at different resonant frequencies, for instance, where such frequencies would inevitably be expressed to differing degrees in different states. The important point is that this variant of the model would, like many such variants (and the real networks recorded for this study), progress through state transitions in a unified manner and that phase coherence would be lower following certain transitions. Although our investigation of the model is limited to recapitulating the state-specific changes in coherence we see in our data, this recapitulation further highlights the aptness of such attractor models for explaining activity in GC and BLA and therefore being good candidates for theoretical investigation to generate predictions about the system to be tested in future experimental work (see below, Discussion).

Ultimately, these simulations demonstrate that a multiregion network can undergo collective, coupled state transitions while having variable functional connectivity during each state. We suggest that the amygdala-cortical system is just such a network.

Discussion

Much of the research that has explored how brain regions work together (Markov et al., 2014; Grabska-Barwińska et al., 2017; Yates et al., 2017; Glaser et al., 2018) makes two broad assumptions, (1) neural responses are identical (save for noise) across repeated stimulus presentations, and (2) neural dynamics evolve on slow time scales (hundreds of milliseconds, or even seconds). These assumptions fail in many cases (Gat et al., 1997; Sugase et al., 1999; Jones et al., 2007; Latimer et al., 2015), including the

present study. In such cases, examination of coupling requires methodologies that can parse sharper changes in neural activity and account for trial-to-trial variability.

In the context of taste processing, GC and BLA form strong candidates for coupling. Both are involved in driving taste-related behavior; perturbations of either results in similar behavioral changes (Lovaglio et al., 2010; Lin et al., 2011, 2018), perturbation of BLA changes GC response dynamics (Piette et al., 2012), and BLA–GC connectivity is important for taste learning (Lin and Reilly, 2012). Furthermore, taste-evoked activity of single neurons in the two structures (Fontanini et al., 2009; Sadacca et al., 2012) undergoes changes (and encoded information) at the same time points.

These facts motivate the current study but stop short of actually testing the hypothesis that BLA and GC transition synchronously. Hitherto, the most direct test of BLA–GC coupling has involved acute optogenetic perturbations of BLA→GC axonal projections (Lin et al., 2021). This perturbation decreased GC ensemble coherence during the transition to palatability coding and reduced palatability relatedness of single-neuron firing following this transition. Brief, bilateral optogenetic perturbation of GC neurons themselves, meanwhile, delivered before or during this transition to palatability coding (Mukherjee et al., 2019), delayed the gaping response of rats to bitter quinine until after the perturbation was removed. Hence, although this GC perturbation hindered planning and execution of the taste motor response, it is likely that the remainder of the circuit maintained output-relevant information, enabling a rebound from the perturbation.

Results of the above studies—the fact that some palatability-related information in GC survives silencing of BLA→GC axons, and the fact that gaping quickly recovers after GC perturbation—in conjunction with the results from the current study, suggest that although BLA and GC are strongly coordinated, they are only parts of an even larger network. This conclusion is further bolstered by work showing that (1) other brain regions show response dynamics similar to BLA and GC (parabrachial nucleus of the pons, Li et al., 2013; lateral hypothalamus, Baez-Santiago et al., 2016), and (2) although palatability responses in GC show a gradient of hedonic values, those in BLA are largely binary (good vs bad; Fontanini et al., 2009; Sadacca et al., 2012). Clearly, there are additional regions (perhaps the lateral hypothalamus) that process palatability information in parallel to BLA to produce the more nuanced coding seen in GC.

In this context, our results are also consistent with those showing that distributed nodes in tightly coupled systems can produce nonidentical coding during stimulus processing and encode redundant information to varying degrees (Siegel et al., 2015; Brincat et al., 2018; Lara et al., 2018; Saravani et al., 2019). This is not truly surprising; complex systems tend to couple on multiple time scales, just as one unit of such a system might increase its spiking while another is silent, and vice versa (Fig. 6*A*), firing of one unit might reflect palatability at one time point, and then the other does so afterward. The fact that palatability relatedness moves from BLA to GC might simply reflect a single cycle of an oscillation.

The advance offered in this study has to do with the subtlety of the predicted coupling, which rendered previously used methodologies for investigating that coupling insufficient. Specifically, we predicted that (trial specific) moments of ensemble state transitions in GC and BLA would be synchronized. This hypothesis could not be tested using analyses that fail to account for dynamics of functional connectivity, collapse data over large time scales (e.g., whole trials), or assume that all trials are dynamically identical. In the current context, such analyses provide misleading information. Both the spike-count correlation and the LFP-phase coherence analyses show BLA and GC to be significantly coordinated but fail to give us any information about temporal dynamics; meanwhile, changes in BLA–GC intertrial phase coherence (which is de rigueur for characterizing inter-regional coupling; Zielinski et al., 2019; Engel et al., 2020; Kramer and Eden, 2020; Zareian et al., 2020) reveal only state-specific reductions in coupling (Fig. 8).

Such state-specific changes in coherence have been seen in transitions between sleep states (Stitt et al., 2017) and between attentive and inattentive states (Siegel et al., 2008). Although the states in evoked activity described in this article are more fleeting than the much longer brain states studied by Stitt et al. (2017) and Siegel et al. (2008), in each case changes in phase coherence mark changes in brain states. Specifically, reductions in coherence such as we observe here have been shown to be associated with intense processing (Supp et al., 2011), whereas increases in coherence are associated with cognitive impairments (Martinet et al., 2017; Arbab et al., 2018). Such low correlations in activity are entirely compatible with strong coupling (Schneidman et al., 2006). Particularly given the fact that BLA–GC phase coherence always stays well above chance levels, it is safe to say that this observation of decreased coherence does not mean that GC and BLA are becoming decoupled at any time point.

Again, had we stopped our analysis at phase coherence, we would have reached the wrong conclusion about amygdala–cortical coupling during taste processing. Only the novel transition coordination analysis (which accounts for both dynamics over the course of the trial and variability across the trials) allowed us to directly test the risky hypothesis that taste processing is characterized by sudden ensemble state transitions shared across BLA and GC. Our successful test of this hypothesis strongly corroborates the results of causal studies showing that wholesale inhibition of BLA (Piette et al., 2012) and precise perturbation of the BLA→GC axonal projection (Lin et al., 2021) specifically perturb processing during—and the transition to—the palatability-related (late) epoch of GC taste coding. This further underscores the limitations of more canonical communication measures with regard to the theories that they are able to test and provides further evidence for the dynamic nature of the BLA–GC interaction.

Together, these results suggest that taste responses observed in BLA and GC are poorly described by feedforward/hierarchical (Parras et al., 2017; Glaser et al., 2018; Heidari-Gorji et al., 2021) models and better described as working in a joint fashion. Our finding of coordinated state transitions is appealingly (if speculatively) explained in terms of collective attractor states (Miller and Katz, 2010, 2013; Litwin-Kumar and Doiron, 2012; La Camera et al., 2019; Recanatesi et al., 2022). Such models require strong, bidirectional connectivity that is observed throughout the taste circuit (Bielavska and Roldan, 1996; McDonald, 1998; Shi and Cassell, 1998) and predict/recapitulate the sharp state transitions that have been reported in GC (Jones et al., 2007; Sadacca et al., 2016), BLA (this study), and other brain regions (Seidemann et al., 1996; Gat et al., 1997; Sugase et al., 1999; Latimer et al., 2015). Another attractive aspect of such a theory is the fact that noise, rather than being a nuisance variable, serves as the force driving state transitions, allowing robust performance in noisy conditions (Miller and Katz, 2013) and explaining the large variability observed in evoked neural and behavioral responses on a trial-by-trial basis (Kisley and Gerstein, 1999; Carandini, 2004; Jones et al., 2007; Sadacca et al., 2016; Kotekal and MacLean, 2020; Peixoto et al., 2021). Given the ubiquity of noise in biological systems (Shadlen and Newsome, 1994, 1998; Miller and Katz, 2010), it seems likely that valid mechanisms of function will be those that have this property.

Of course, causal confirmation of this theory waits on evidence that the two structures influence one another recurrently, that is, studies investigating the role of the GC→BLA (reverse) projection in taste processing. Although the GC→BLA projection has been shown to be important for taste-related learning, (Lavi et al., 2018; Kayyal et al., 2019), its role in generating passive taste responses is yet to be elucidated. If recurrent circuitry plays a role in taste processing, perturbation of the GC→BLA projection should change not only activity in BLA but also the source activity in GC, reflecting the fact that the circuit processes information in a loop fashion. Such an outcome would further drive home the value of moving away from feedforward biases in the study of taste processing.

Ultimately, a nuanced understanding of inter-region communication and of how this communication is important for generating behavioral output will require that we appreciate the sorts of nonlinearities and variability examined here, that we do not smooth out potentially important sudden ensemble changes in real-time ensemble activity. The current study furthers our trial-specific understanding of neural activity and will hopefully drive further questions regarding the role of reciprocal connectivity and metastable dynamics in sensory processing.

References

Ames KC, Churchland MM (2019) Motor cortex signals for each arm are mixed across hemispheres and neurons yet partitioned within the population response. Elife 8:e46159.

Antzoulatos EG, Miller EK (2016) Synchronous beta rhythms of frontoparietal networks support only behaviorally relevant representations. Elife 5: e17822.

Arbab T, Battaglia FP, Pennartz CMA, Bosman CA (2018) Abnormal hippocampal theta and gamma hypersynchrony produces network and spike timing disturbances in the Fmr1-KO mouse model of Fragile X syndrome. Neurobiol Dis 114:65–73.

Arce-McShane FI, Ross CF, Takahashi K, Sessle BJ, Hatsopoulos NG (2016) Primary motor and sensory cortical areas communicate via spatiotemporally coordinated networks at multiple frequencies. Proc Natl Acad Sci U S A 113:5083–5088.

Averbeck BB, Sohn J-W, Lee D (2006a) Activity in prefrontal cortex during dynamic selection of action sequences. Nat Neurosci 9:276–282.

Averbeck BB, Latham PE, Pouget A (2006b) Neural correlations, population coding and computation. Nat Rev Neurosci 7:358–366.

Baez-Santiago MA, Reid EE, Moran A, Maier JX, Marrero-Garcia Y, Katz DB (2016) Dynamic taste responses of parabrachial pontine neurons in awake rats. J Neurophysiol 115:1314–1323.

Bastos AM, Vezoli J, Bosman CA, Schoffelen J-M, Oostenveld R, Dowdall JR, De Weerd P, Kennedy H, Fries P (2015) Visual areas exert feedforward and feedback influences through distinct frequency channels. Neuron 85:390–401.

Baxter MG, Croxson PL (2012) Facing the role of the amygdala in emotional information processing. Proc Natl Acad Sci U S A 109:21180–21181.

Bielavska E, Roldan G (1996) Ipsilateral connections between the gustatory cortex, amygdala and parabrachial nucleus are necessary for acquisition and retrieval of conditioned taste aversion in rats. Behav Brain Res 81:25–31.

Blei DM, Kucukelbir A, McAuliffe JD (2017) Variational inference: a review for statisticians. J Am Stat Assoc 112:859–877.

Brincat SL, Siegel M, von Nicolai C, Miller EK (2018) Gradual progression from sensory to task-related processing in cerebral cortex. Proc Natl Acad Sci U S A 115:E7202–E7211.

Carandini M (2004) Amplification of trial-to-trial response variability by neurons in visual cortex. PLOS Biol 2:e264.

Clarke SNDA, Ossenkopp K-P (1998) Taste reactivity responses in rats: influence of sex and the estrous cycle. Am J Physiol 274:R718–R724.

Di Lorenzo PM, Monroe S (1997) Transfer of information about taste from the nucleus of the solitary tract to the parabrachial nucleus of the pons. Brain Res 763:167–181.

Edelman GM, Gally JA (2013) Reentry: a key mechanism for integration of brain function. Front Integr Neurosci 7:63.

Engel D, Schütz A, Krala M, Schwenk JCB, Morris AP, Bremmer F (2020) Inter-trial phase coherence of visually evoked postural responses in virtual reality. Exp Brain Res 238:1177–1189.

Fontanini A, Katz DB (2006) State-dependent modulation of time-varying gustatory responses. J Neurophysiol 96:3183–3193.

Fontanini A, Grossman SE, Figueroa JA, Katz DB (2009) Distinct subtypes of basolateral amygdala taste neurons reflect palatability and reward. J Neurosci 29:2486–2495.

Fu J-Y, Yu X-D, Zhu Y, Xie S-Z, Tang M-Y, Yu B, Li X-M (2020) Whole-brain map of long-range monosynaptic inputs to different cell types in the amygdala of the mouse. Neurosci Bull 36:1381–1394.

Gal-Ben-Ari S, Rosenblum K (2012) Molecular mechanisms underlying memory consolidation of taste information in the cortex. Front Behav Neurosci 5:87.

Gat I, Tishby N, Abeles M (1997) Hidden Markov modeling of simultaneously recorded cells in the associative cortex of behaving monkeys. Network: Comput Neural Syst 8:297–322.

Glaser JI, Perich MG, Ramkumar P, Miller LE, Kording KP (2018) Population coding of conditional probability distributions in dorsal premotor cortex. Nat Commun 9:1788.

Grabska-Barwińska A, Barthelmé S, Beck J, Mainen ZF, Pouget A, Latham PE (2017) A probabilistic approach to demixing odors. Nat Neurosci 20:98–106.

Grossman SE, Fontanini A, Wieskopf JS, Katz DB (2008) Learning-related plasticity of temporal coding in simultaneously recorded amygdala–cortical ensembles. J Neurosci 28:2864–2873.

Haley MS, Fontanini A, Maffei A (2016) Laminar- and target-specific amygdalar inputs in rat primary gustatory cortex. J Neurosci 36:2623–2637.

Heidari-Gorji H, Ebrahimpour R, Zabbah S (2021) A temporal hierarchical feedforward model explains both the time and the accuracy of object recognition. Sci Rep 11:5640.

Jones LM, Fontanini A, Katz DB (2006) Gustatory processing: a dynamic systems approach. Curr Opin Neurobiol 16:420–428.

Jones LM, Fontanini A, Sadacca BF, Miller P, Katz DB (2007) Natural stimuli evoke dynamic sequences of states in sensory cortical ensembles. Proc Natl Acad Sci U S A 104:18772–18777.

Katz DB, Simon SA, Nicolelis MAL (2001) Dynamic and multimodal responses of gustatory cortical neurons in awake rats. J Neurosci 21:4478–4489.

Kayyal H, Yiannakas A, Chandran SK, Khamaisy M, Sharma V, Rosenblum K (2019) Activity of insula to basolateral amygdala projecting neurons is necessary and sufficient for taste valence representation. J Neurosci 39:9369–9382.

Kietzmann TC, Spoerer CJ, Sörensen LKA, Cichy RM, Hauk O, Kriegeskorte N (2019) Recurrence is required to capture the representational dynamics of the human visual system. Proc Natl Acad Sci U S A 116:21854–21863.

Kisley MA, Gerstein GL (1999) Trial-to-trial variability and state-dependent modulation of auditory-evoked responses in cortex. J Neurosci 19:10451–10460.

Kotekal S, MacLean JN (2020) Recurrent interactions can explain the variance in single trial responses. PLOS Comput Biol 16:e1007591.

Kramer MA, Eden UT (2020) Case studies in neural data analysis. Cambridge, MA: MIT. Available at https://mark-kramer.github.io/Case-Studies-Python/05.html.

Kucukelbir A, Tran D, Ranganath R, Gelman A, Blei DM (2016) Automatic differentiation variational inference. J Mach Learn Res 18:430–474.

La Camera G, Fontanini A, Mazzucato L (2019) Cortical computations via metastable activity. Curr Opin Neurobiol 58:37–45.

Lara AH, Cunningham JP, Churchland MM (2018) Different population dynamics in the supplementary motor area and motor cortex during reaching. Nat Commun 9:2754.

Latimer KW, Yates JL, Meister MLR, Huk AC, Pillow JW (2015) Single-trial spike trains in parietal cortex reveal discrete steps during decision-making. Science 349:184–187.

Lavi K, Jacobson GA, Rosenblum K, Lüthi A (2018) Encoding of conditioned taste aversion in cortico-amygdala circuits. Cell Rep 24:278–283.

Li JX, Yoshida T, Monk KJ, Katz DB (2013) Lateral hypothalamus contains two types of palatability-related taste responses with distinct dynamics. J Neurosci 33:9462–9473.

Li JX, Maier JX, Reid EE, Katz DB (2016) Sensory cortical activity is related to the selection of a rhythmic motor action pattern. J Neurosci 36:5596–5607.
Lin J-Y, Reilly S (2012) Amygdala–gustatory insular cortex connections and taste neophobia. Behav Brain Res 235:182–188.
Lin J-Y, Arthurs J, Reilly S (2011) Role of the insular cortex in morphine-induced conditioned taste avoidance. Brain Res 1384:80–88.
Lin J-Y, Arthurs J, Reilly S (2015) Gustatory insular cortex, aversive taste memory and taste neophobia. Neurobiol Learn Mem 119:77–84.
Lin J-Y, Arthurs J, Reilly S (2018) The effects of amygdala and cortical inactivation on taste neophobia. Neurobiol Learn Mem 155:322–329.
Lin J-Y, Mukherjee N, Bernstein MJ, Katz DB (2021) Perturbation of amygdala-cortical projections reduces ensemble coherence of palatability coding in gustatory cortex. Elife 10:e65766.
Litwin-Kumar A, Doiron B (2012) Slow dynamics and high variability in balanced cortical networks with clustered connections. Nat Neurosci 15:1498–1505.
Lovaglio J, Lin J-Y, Roman C, Reilly S (2010) Basolateral amygdala and morphine-induced taste avoidance in the rat. Physiol Behav 99:419–423.
Lundqvist M, Bastos AM, Miller EK (2020) Preservation and changes in oscillatory dynamics across the cortical hierarchy. J Cogn Neurosci 32:2024–2035.
Maass W, Joshi P, Sontag ED (2007) Computational aspects of feedback in neural circuits. PLOS Comput Biol 3:e165.
Mante V, Sussillo D, Shenoy KV, Newsome WT (2013) Context-dependent computation by recurrent dynamics in prefrontal cortex. Nature 503:78–84.
Markov NT, Vezoli J, Chameau P, Falchier A, Quilodran R, Huissoud C, Lamy C, Misery P, Giroud P, Ullman S, Barone P, Dehay C, Knoblauch K, Kennedy H (2014) Anatomy of hierarchy: feedforward and feedback pathways in macaque visual cortex. J Comp Neurol 522:225–259.
Martinet L-E, Fiddyment G, Madsen JR, Eskandar EN, Truccolo W, Eden UT, Cash SS, Kramer MA (2017) Human seizures couple across spatial scales through travelling wave dynamics. Nat Commun 8:14896.
Mazzucato L, Fontanini A, Camera GL (2015) Dynamics of multistable states during ongoing and evoked cortical activity. J Neurosci 35:8214–8231.
McDonald AJ (1998) Cortical pathways to the mammalian amygdala. Prog Neurobiol 55:257–332.
Miller P, Katz DB (2010) Stochastic transitions between neural states in taste processing and decision-making. J Neurosci 30:2559–2570.
Miller P, Katz DB (2013) Accuracy and response-time distributions for decision-making: linear perfect integrators versus nonlinear attractor-based neural circuits. J Comput Neurosci 35:261–294.
Moran A, Katz DB (2014) Sensory cortical population dynamics uniquely track behavior across learning and extinction. J Neurosci 34:1248–1257.
Mukherjee N, Wachutka J, Katz DB (2017) Python meets systems neuroscience: affordable, scalable and open-source electrophysiology in awake, behaving rodents. Paper presented at the 16th Python in Science Conference, Austin, TX, USA.
Mukherjee N, Wachutka J, Katz DB (2019) Impact of precisely-timed inhibition of gustatory cortex on taste behavior depends on single-trial ensemble dynamics. Elife 8:e45968.
Parras GG, Nieto-Diego J, Carbajal GV, Valdés-Baizabal C, Escera C, Malmierca MS (2017) Neurons along the auditory pathway exhibit a hierarchical organization of prediction error. Nat Commun 8:2148.
Paxinos G (2007) The rat brain in stereotaxic coordinates. Burlington MA: Elsevier.
Pedregosa F, Varoquaux G, Gramfort A, Michel V, Thirion B, Grisel O, Blondel M, Prettenhofer P, Weiss R, Dubourg V, Vanderplas J, Passos A, Cournapeau D, Brucher M, Perrot M, Duchesnay É (2011) Scikit-learn: machine Learning in Python. J Mach Learn Res 12:2825–2830.
Peixoto D, Verhein JR, Kiani R, Kao JC, Nuyujukian P, Chandrasekaran C, Brown J, Fong S, Ryu SI, Shenoy KV, Newsome WT (2021) Decoding and perturbing decision states in real time. Nature 591:604–609.
Piette CE, Baez-Santiago MA, Reid EE, Katz DB, Moran A (2012) Inactivation of basolateral amygdala specifically eliminates palatability-related information in cortical sensory responses. J Neurosci 32:9981–9991.
Place R, Farovik A, Brockmann M, Eichenbaum H (2016) Bidirectional prefrontal-hippocampal interactions support context-guided memory. Nat Neurosci 19:992–994.
Press WH, Teukolsky SA (1990) Savitzky–Golay smoothing filters. Comput Phys 4:669.
Rabiner LR (1989) A tutorial on hidden Markov models and selected applications in speech recognition. Proc IEEE 77:257–286.
Raichle ME (2015) The brain's default mode network. Annu Rev Neurosci 38:433–447.
Recanatesi S, Pereira-Obilinovic U, Murakami M, Mainen Z, Mazzucato L (2022) Metastable attractors explain the variable timing of stable behavioral action sequences. Neuron 110:139–153.e9.
Sadacca BF, Rothwax JT, Katz DB (2012) Sodium concentration coding gives way to evaluative coding in cortex and amygdala. J Neurosci 32:9999–10011.
Sadacca BF, Mukherjee N, Vladusich T, Li JX, Katz DB, Miller P (2016) The behavioral relevance of cortical neural ensemble responses emerges suddenly. J Neurosci 36:655–669.
Salvatier J, Wiecki TV, Fonnesbeck C (2016) Probabilistic programming in Python using PyMC3. PeerJ Comput Sci 2:e55.
Saravani AG, Forseth KJ, Tandon N, Pitkow X (2019) Dynamic brain interactions during picture naming. eNeuro 6:ENEURO.0472-18.2019.
Seidemann E, Meilijson I, Abeles M, Bergman H, Vaadia E (1996) Simultaneously recorded single units in the frontal cortex go through sequences of discrete and stable states in monkeys performing a delayed localization task. J Neurosci 16:752–768.
Schneidman E, Berry MJ 2nd, Segev R, Bialek W (2006) Weak pairwise correlations imply strongly correlated network states in a neural population. Nature 440:1007–1012.
Seitzman BA, Snyder AZ, Leuthardt EC, Shimony JS (2019) The state of resting state networks. Top Magn Reson Imaging 28:189–196.
Shadlen MN, Newsome WT (1994) Noise, neural codes and cortical organization. Curr Opin Neurobiol 4:569–579.
Shadlen MN, Newsome WT (1998) The variable discharge of cortical neurons: implications for connectivity, computation, and information coding. J Neurosci 18:3870–3896.
Shi C-J, Cassell MD (1998) Cortical, thalamic, and amygdaloid connections of the anterior and posterior insular cortices. J Comp Neurol 399:440–468.
Siegel M, Donner TH, Oostenveld R, Fries P, Engel AK (2008) Neuronal synchronization along the dorsal visual pathway reflects the focus of spatial attention. Neuron 60:709–719.
Siegel M, Buschman TJ, Miller EK (2015) Cortical information flow during flexible sensorimotor decisions. Science 348:1352–1355.
Stitt I, Hollensteiner KJ, Galindo-Leon E, Pieper F, Fiedler E, Stieglitz T, Engler G, Nolte G, Engel AK (2017) Dynamic reconfiguration of cortical functional connectivity across brain states. Sci Rep 7:8797.
Sugase Y, Yamane S, Ueno S, Kawano K (1999) Global and fine information coded by single neurons in the temporal visual cortex. Nature 400:869–873.
Supp GG, Siegel M, Hipp JF, Engel AK (2011) Cortical hypersynchrony predicts breakdown of sensory processing during loss of consciousness. Curr Biol 21:1988–1993.
Travers JB, Norgren R (1986) Electromyographic analysis of the ingestion and rejection of sapid stimuli in the rat. Behav Neurosci 100:544–555.
Vallat R (2018) Pingouin: statistics in Python. J Open Source Softw 3:1026.
Virtanen P, et al. (2020) SciPy 1.0: fundamental algorithms for scientific computing in Python. Nat Methods 17:261–272.
Yamamoto T (2008) Central mechanisms of taste: cognition, emotion and taste-elicited behaviors. Jpn Dent Sci Rev 44:91–99.
Yates JL, Park IM, Katz LN, Pillow JW, Huk AC (2017) Functional dissection of signal and noise in MT and LIP during decision-making. Nat Neurosci 20:1285–1292.
Zandvakili A, Kohn A (2015) Coordinated neuronal activity enhances corticocortical communication. Neuron 87:827–839.
Zareian B, Maboudi K, Daliri MR, Abrishami Moghaddam H, Treue S, Esghaei M (2020) Attention strengthens across-trial pre-stimulus phase coherence in visual cortex, enhancing stimulus processing. Sci Rep 10:4837.
Zielinski MC, Shin JD, Jadhav SP (2019) Coherent coding of spatial position mediated by theta oscillations in the hippocampus and prefrontal cortex. J Neurosci 39:4550–4565.